Structure of a volume-regulated anion channel of the LRRC8 family

Deneka, Dawid ; Sawicka, Marta ; Lam, Andy K M ; Paulino, Cristina ; Dutzler, Raimund

Abstract: Volume-regulated anion channels are activated in response to hypotonic stress. These channels are composed of closely related paralogues of the leucine-rich repeat-containing protein 8 (LRRC8) family that co-assemble to form hexameric complexes. Here, using cryo-electron microscopy and X-ray crystallography, we determine the structure of a homomeric channel of the obligatory subunit LRRC8A. This protein conducts ions and has properties in common with endogenous heteromeric channels. Its modular structure consists of a transmembrane pore domain followed by a cytoplasmic leucine-rich repeat domain. The transmembrane domain, which is structurally related to connexin proteins, is wide towards the cytoplasm but constricted on the outside by a structural unit that acts as a selectivity filter. An excess of basic residues in the filter and throughout the pore attracts anions by electrostatic interaction. Our work reveals the previously unknown architecture of volume-regulated anion channels and their mechanism of selective anion conduction.

DOI: https://doi.org/10.1038/s41586-018-0134-y

Structure of a volume-regulated anion channel of the LRRC8 family

Dawid Deneka[1*], Marta Sawicka[1*], Andy K. M. Lam[1], Cristina Paulino[1]† and Raimund Dutzler[1]

[1] Department of Biochemistry University of Zurich, Winterthurer Str. 190, CH-8057 Zurich, Switzerland

† Present Address, Department of Structural Biology at the Groningen Biomolecular Sciences and Biotechnology Institute, University of Groningen, Nijenborgh 7, 9747 AG Groningen, The Netherlands

* Both authors contributed equally to this work

Volume-regulated anion channels (VRACs) are activated in response to hypotonic stress. These channels are composed of closely related paralogs of the LRRC8 family, which co-assemble to form hexameric complexes. Here we describe the structure of a homomeric channel of the obligatory subunit LRRC8A determined by cryo-electron microscopy and X-ray crystallography. This protein conducts ions and shares properties of endogenous heteromeric channels. Its modular structure consists of a transmembrane pore domain followed by a cytoplasmic leucine-rich repeat domain. The transmembrane domain, which is related to connexins, is wide towards the cytoplasm but constricted on the outside by a structural unit that acts as a selectivity filter. Anions are attracted by the positive electrostatics, in the filter and throughout the pore, conferred by an excess of basic residues. Our work reveals the previously unknown architecture of VRACs and their mechanism of selective anion conduction.

Volume-regulated anion channels (VRACs) are important constituents of the cellular response to osmotic swelling[1]. This process occurs as a consequence of aquaporin-mediated water influx into cells under hypotonic conditions. To counteract the volume increase and prevent swelling-induced burst, different ion transport proteins are activated, which allows for a controlled efflux of ions, organic osmolytes and consequently water to return to their original unchallenged state[2]. The proteins involved in such regulatory volume decrease (RVD) include cation-selective ion channels, secondary-active transporters and VRACs[1]. Besides their role in RVD, VRACs were also proposed to participate in apoptosis[3] and in the regulation of electric excitability of neurons through the release of neurotransmitters from astrocytes[4-6]. Although investigated by electrophysiology for decades[3,7], the molecular identity of VRACs has been unknown until 2014, when two groups independently identified LRRC8A as an essential component of the channel[8,9]. LRRC8A is a member of a protein family found exclusively in vertebrates. In mammals the family encompasses five paralogs (LRRC8A–E), all of which share a high degree of sequence similarity[10-12] (Extended Data Fig. 1a). The 796 to 858 residue proteins consist of a transmembrane domain that is remotely related to pannexins[12], followed by a C-terminal domain containing 15-17 predicted leucine-rich repeats (LRR)[11,12]. Since LRR domains participate in ligand binding in various receptors on the extracellular side[13,14], a similar arrangement was initially hypothesized for the LRRC8 family[11]. This proposal was later refuted by biochemical studies investigating the topology of the family that have placed both termini on the cytoplasmic side[8,9,15]. LRRC8 proteins are widely expressed and form heteromeric channels of diverse subunit stoichiometry and distinct functional properties[8,9]. Though some assemblies are selective for anions, others are also permeable to osmolytes, amino acids and neurotransmitters or are involved in the uptake of anticancer drugs[6,8,9,16-18]. Whereas LRRC8A is the only obligatory subunit of VRACs[8,9], there is presently no evidence of endogenous homomeric channels in a physiological context. However, when overexpressed on its own, LRRC8A is targeted to the plasma membrane[9] and was reported to form oligomers of similar size as heteromeric assemblies composed of different paralogs, but with smaller conductance[18]. We thus expect a homomeric VRAC, containing the LRRC8A subunit only, to exhibit very similar structural properties as LRRC8 heteromers, while circumventing the problem of a variable subunit stoichiometry. The latter would increase the heterogeneity of the sample and impede an unambiguous structure determination.

Here we describe the structure of the homomeric LRRC8A complex determined by cryo-electron microscopy (cryo-EM) and the X-ray structure of its isolated cytoplasmic domain. The structure reveals the general architecture of a VRAC and, in combination with functional experiments, provides insight into the mechanism of selective anion conduction.

Structure determination and functional characterization

For our investigations of the molecular properties of VRACs we have studied mouse paralogs of the LRRC8 family. To recapitulate the functional behavior of homo- and heteromeric constructs, we have recorded currents from a human embryonic kidney (HEK) cell-line not expressing endogenous LRRC8 subunits (*LRRC8*$^{-/-}$)[9,17]. Native HEK cells show large anion-selective currents in response to a decrease of the intracellular ion concentration, which are absent in *LRRC8*$^{-/-}$ (Extended Data Fig. 2a–e), thus confirming that VRAC function is mediated by LRRC8 proteins, which are activated at low cytoplasmic ionic strength[18,19]. As described previously[9], the co-transfection of *LRRC8*$^{-/-}$ cells with DNA coding for mLRRC8A and C (mLRRC8A/C) restores the native-like current response (Fig. 1a, b Extended Data Fig. 2f, g). Similarly, currents with much smaller amplitude and stronger outward rectification are evoked after transfection with mLRRC8A alone despite a similar surface expression of the protein (Fig. 1a, c, Extended Data Fig. 2h–j). As for native cells and the mLRRC8A/C constructs, these currents are also activated by a decreased intracellular ion concentration, although with lower sensitivity (Fig. 1c), thus confirming that mLRRC8A forms functional channels with seemingly poor conduction properties. For structure determination of a VRAC, we have transiently expressed mLRRC8A in HEK293S-GnTI^{-} cells. Consistent with previous observations[18], the purified homomeric proteins form hexamers, the expected oligomeric state of the family[12] (Extended Data Fig. 2k). The mLRRC8A subunit encompasses 810 residues and contains a 344 amino acid-long transmembrane pore domain followed by a 466 amino acid-long cytoplasmic part (Extended Data Fig. 1). The modularity of its organization is underlined by the possibility to express and purify both domains as separate stable entities with the transmembrane pore domain (mLRRC8A^{PD}) retaining its oligomeric structure and the isolated cytoplasmic LRR domain (mLRRC8A^{LRRD}) dissociating into monomers (Extended Data Fig. 2k-m).

Two datasets of the mLRRC8A protein at high ionic strength, recorded by cryo-EM at different microscopes, reveal the detailed structural properties of the channel (Extended Data Fig. 3 and 4). When viewed from within the membrane, the elongated particles exhibit distinct features corresponding to the transmembrane pore domain (PD) and the cytoplasmic LRR domain (LRRD). As expected from size exclusion chromatography, mLRRC8A forms hexamers. 3D classification revealed a well-defined symmetric PD and larger structural heterogeneity in the LRRD, indicating a higher flexibility of this region (Extended Data Figs. 3d and 4d). A major class shows a channel in which the C6 symmetry of the transmembrane pore domain lowers to a three-fold relationship between pairs of LRRDs. However, even for C3-symmetric particles, the density of the cytoplasmic unit is considerably weaker and of lower resolution compared to the transmembrane domain (Extended Data Fig. 3f, 4f and 5a, b). The general structural properties of full-length mLRRC8A were also observed in the 7.9 Å cryo-EM density of heteromeric channels consisting of the closely related mLRRC8A and C subunits, which confirms that the structure observed for mLRRC8A hexamers is representative for the entire protein family (Fig. 1d, e, Extended Data Figs. 1 and 5c–h).

The detailed molecular structure of mLRRC8A was determined from different datasets. The structure of the PD was built into a 3.66 Å map obtained from high-resolution cryo-EM data after masking and imposing of C6 symmetry (Extended Data Figs. 4d, g, h and 6a–c). The isolated LRRD was crystallized and its structure was determined by X-ray crystallography at 1.8 Å (Extended Data Figs. 6d, e and 7a). The full-length protein was finally assembled from its two parts into C3-symmetrized cryo-EM density of the entire channel at 4.25 Å and into a second independent reconstruction at 5.0 Å with better-defined density of the cytoplasmic domains (Extended Data Figs. 3e, f, 4e, f, 5a, b and 6f, g). In combination, this procedure allowed an unambiguous interpretation of the protein structure by an atomic model (Fig. 2, Extended Data Fig. 7).

mLRRC8A structure

The mLRRC8A structure shows a hexameric protein that is 180 Å long and 110 Å wide (Fig. 2). The six subunits are arranged around an axis of symmetry that defines the ion conduction path with their N- and C-termini located on the cytoplasmic side and facing the lumen (Fig. 2 and 3a). The PD of each subunit contains four transmembrane helices (TM1-TM4) with long interspersed regions folding into compact structures that constitute the extra- and intracellular entrances to the pore (Fig. 3b, Extended Data Fig. 1). The general resemblance of the PD to gap junction proteins is reflected in the low RMSD of 1.7 Å and 2.3 Å calculated from the superposition of the membrane-inserted helices of mLRRC8A with connexin[20] and innexin[21] subunits respectively (Fig. 3c). The cytoplasmic LRRD shares close structural similarity with related units in other proteins[13] (Fig. 3d). As predicted from its sequence, it consists of 16 structural repeats each containing a β-strand followed by an α-helix of variable length (Fig. 3e, Extended Data Fig. 1). As is characteristic for domains exhibiting this fold, the interacting strands form a parallel β-sheet at the concave side of the horseshoe-shaped protein[13], which faces the symmetry axis in the oligomeric channel (Fig. 2a). Both terminal repeats are capped by single helices, which connect to the pore domain on the N-terminus and which contribute to the interaction with LRRDs of other subunits at the C-terminus (Fig. 3e).

The pore domain

The six-fold symmetric pore of the hexameric channel can be divided into three segments: a central, approximately 50 Å-long transmembrane part (TM), and two flanking sub-domains which protrude 25 Å from the membrane towards the cytoplasm and the extracellular side (Fig. 4a). Whereas the extra- and intracellular components of the pore are hydrophilic and contain multiple charged residues, the wide transmembrane region is dominated by hydrophobic residues (Fig. 4a). Interactions between the PDs of neighboring subunits bury 3,700 Å^2 of the

combined molecular surface and are particularly tight outside of the membrane (Fig. 4a). The extracellular sub-domain (ESD) is comprised of the E1 and E2 regions (according to the innexin nomenclature[21,22]), which fold into an α-helix (E1H) and a three-stranded anti-parallel β-sheet (E1β, E2β1 and E2β2, Fig. 3b, Extended Data Fig. 1). Part of the extended loop connecting E1β and E1H, which carries glycosylation sites[9], is not defined in the cryo-EM density. The ESD, which is stabilized by three disulfide bridges, harbors the narrowest part of the ion conduction path, with a radius of about 2.9 Å at its constriction (Fig. 4a–c, Extended Data Fig. 6b, c). In the membrane-inserted region, the conical pore widens and is lined by residues of TM1 throughout its length and additionally by residues of TM2 on its intracellular half (Figs. 3a, b and 4b). Within this region, the interface between subunits is less tightly packed and contains gaps that are probably sealed by lipids (Fig. 4a). On the cytoplasmic side, a sub-domain (CSD) containing six α-helices (contributed by the cytoplasmic loop CL and the c-terminal region CT according to the innexin nomenclature) constitutes the channel exit leading to the cytoplasmic LRRDs (Figs. 3a, b, 4a, b, Extended Data Fig. 1). The CL region also harbors an unstructured loop containing several phosphorylation sites[23,24] (Extended Data Fig. 1). Within the TM and the CSD the pore is wide, extending up to 32 Å in diameter. However, since the first 14 residues of the N-terminus of each subunit located close to the intracellular membrane boundary and projecting to the pore lumen are not defined in the structure, the dimensions of this part of the ion conduction path cannot be defined with certainty.

Organization of the LRR domains

Below the CSD, the wide, protein-enclosed exit of the pore leads into a 80 Å-long structure that is formed by the cytoplasmic LRRDs (Figs. 2a, 3a). In the mLRRC8A hexamer, these cytoplasmic units are tilted by about 30º–40º with respect to the pore axis towards the plane of the membrane (Figs. 2b and 5a). The six LRR domains do not interact in the same way, but rather form a trimer of dimers, resulting in a large interface between interacting pairs of LRR domains (referred to as l- and r-subunits) that bury more than 1,603 $Å^2$ of the combined molecular surface, and a small interface of the C-terminal α-helix of the r-subunit with the l-subunit of a neighboring domain pair burying 288 $Å^2$ (Fig. 5b-d). The tight interactions observed between pairs of LRR domains cause a change in the orientation of adjacent cytoplasmic domains that can be approximated by a 42º rotation relative to each other (Fig. 5a). This leads to a breakdown of the C6 symmetry, observed for the pore region, to an overall three-fold symmetry (Fig. 5d). At the intracellular end, the C-terminal α-helices of the three l-subunits engage in mutual interactions at the location of the symmetry axis (Fig. 5d). Potential entry pathways for Cl^- ions are created by spacious, up to 12 Å large fenestrations at the small interface between domain pairs that would presumably allow hydrated anions to access the pore region (Fig. 5b, d). On their entire surface, the LRR domains are highly hydrophilic (Fig. 5e).

The interaction interfaces bury multiple ionizable residues, suggesting that the affinity of these interactions might be affected by ionic strength.

Electrostatics and selectivity filter

The analysis of the electrostatic properties of the pore region sheds light on the observed selectivity for anions. The homomeric channel consisting of mLRRC8A subunits exhibits a strongly positive electrostatic potential throughout the ion conduction path with a maximum at the constriction located at the extracellular side (Fig. 6a, b, Extended Data Fig. 8a, b). The general features of the pore potential (calculated from a homology model) are preserved in a heteromeric channel consisting of a hypothetical arrangement of alternating A and C subunits, thus suggesting that anions are attracted by coulombic interactions in both, homomeric and heteromeric proteins, (Fig. 6a, Extended Data Fig. 8b). During permeation, the constriction of the ESD may act as a filter, selecting for the size and charge of partially dehydrated anions. At this narrowing, located at the N-terminus of α-helix E1H, the filter contains an arginine (R103) whose side chain points towards the pore axis (Fig. 6c, d, Extended Data Fig. 6c). Remarkably, the equivalent positions in other paralogs (except for mLRRC8B) are uncharged, thus accounting for the lower positive electrostatics at the extracellular pore entrance observed for the mLRRC8A/C model (Fig. 6a, Extended Data Figs. 1a and 8b). In the case of mLRRC8C and E, they contain a leucine residue, which, in a heteromeric channel, might widen the pore and change the structural flexibility of the filter (Extended Data Fig. 8c, d). Towards the cytoplasmic end of the ESD, two additional basic residues (H104 and K51) may also contribute to the positive electrostatic environment in the narrow pore region (Fig. 6a–d). However, whereas K51 is conserved and likely carries a positive net charge, H104 is only present in the A subunit and might, due to its proximity to R103, not be protonated. Upstream of R103 are K98 and D100, two residues involved in mutual inter-subunit interactions, were described to alter the inactivation of the channel at positive voltages and were thus postulated to line the permeation path[25] (Fig. 6c, d). In intracellular direction, close to the membrane boundary, a second narrowing of larger diameter exposes two threonines (T48 and T44) into the pore region (Fig. 6b). The mutation of T44 to cysteine has previously been described to alter the selectivity between anions and lower the pore conductance upon modification with negatively charged thiol-reactive reagents[8]. Although this region is too wide for coordination of dehydrated ions, interactions might be mediated via solvating waters. Notably, residual density in the cryo-EM map in proximity to both threonines could hint at the presence of hydrated anions (Extended Data Fig. 8e). Intracellular to T44, the pore widens further and turns predominantly hydrophobic before it becomes hydrophilic again at the intracellular sub-domain, where an excess of basic residues renders the electrostatics attractive for anions entering the channel from the intracellular side (Figs. 4a and 6a).

Structure-function relationships

It is possible that the presence of six arginine residues at the extracellular constriction of the mLRRC8A pore might sterically impede ion conduction, thus accounting for the poor functional response of the homomeric channel. To address this question, we investigated whether the mutation of R103A in mLRRC8A would increase the conductance and thus restore the functional phenotype of heteromeric channels. However, the truncation of this bulky side chain was insufficient to increase the current density of mLRRC8A(R103A) (Extended Data Fig. 9a–b). We next examined the mutation L105R in the C subunit of the heteromeric mLRRC8A/C(L105R) channel, which mimics the ring of six arginines at the narrowest constriction in the mLRRC8A homomer. Consistent with the above result, we observed very similar current response as in WT channels, which provides further evidence that a high density of arginine residues at the pore constriction does not prevent ion conduction (Extended Data Fig. 9c–d). Finally, we paired the mLRRC8A(R103A) subunit with the mLRRC8C subunit and found decreased but still sizable currents upon lowering of the intracellular ionic strength for this construct not containing any arginines at the constriction (Extended Data Fig. 9e-f). Nonetheless, in contrast to the highly anion-selective currents mediated by mLRRC8A/C and mLRRC8A/C(L105R), mLRRC8A(R103A)/C shows measurable Na^+ permeability (Fig. 6e, Extended Data Fig. 9g-h), which demonstrates that presence of constricting arginines plays an important role in determining the charge selectivity of the mLRRC8 channels. The general preference for anions in the mutant not containing any arginines at the constriction is likely conferred by other positively charged residues distributed along the pore (Fig. 4a and 6a, Extended Data Fig. 8b, f). The importance of this location for anion interactions is also reflected in the positive correlation of the arginine density with sulfate permeability, which is consistent with the presence of a weak anion binding site at the position of the constriction (Fig. 6e, Extended Data Fig. 9i-n). Together, these experiments demonstrate the functional importance of the narrow extracellular region that acts as a selectivity filter and mediates anion conduction.

Discussion

In our study, we have elucidated the molecular architecture of volume-regulated anion channels of the LRRC8 family and investigated its relationship to functional properties. VRACs are hexameric proteins of modular structure consisting of a transmembrane pore domain and a cytoplasmic LRR domain (Figs. 2, and 6g). A characteristic feature of their organization, is the symmetry mismatch between the six-fold symmetric PDs and the three fold symmetric LRRDs akin to a break of symmetry observed in ionotropic glutamate receptors[26]. The loss of symmetry in the LRRDs in a fraction of the particles underlines their intrinsic mobility and resembles a

similar case found in the magnesium channel CorA[27]. Though unrelated in sequence, the structure of the PD resembles gap junction channels, particularly with respect to the location of the transmembrane helices and the general organization of the ESD (Fig. 3c, Extended Data Fig. 10a, b). Despite their structural resemblance, the two protein classes exhibit distinct functional features, with gap junctions forming wide channels of poor selectivity that also permit the diffusion of larger substrates[28,29], and certain VRAC channels (such as channels composed of LRRC8A and C subunits) being selective for smaller anions, with a negligible conductance for cations[30] (Fig. 6e, Extended Data Figs. 2c, 9g, h). A comparison of their structures sheds light on their distinct permeation properties (Extended Data Fig. 10). Besides the difference in the electrostatics, with a strong positive potential being a unique property of VRACs (Fig. 6a), connexins[20,22] and invertebrate innexins[21] form channels of large diameter throughout, whereas VRAC channels are constricted at their extracellular part (Fig. 4b, c, Extended Data Fig. 10c–f). In both gap junction proteins, the N-terminus constricts the wide channels by forming an α-helix that lines the pore and projects towards the extracellular direction (Extended Data Fig. 10a, b, e, f)[20–22]. In contrast, the equivalent part of LRRC8A channels, although of similar length, was not defined in the cryo-EM density. Thus, while the N-terminus of connexins was implicated in the gating of gap junctions[20], the involvement of the N-terminus of LRRC8 proteins in channel regulation is currently unclear.

The structure of the ESD of the VRAC pore resembling a size and charge selectivity filter that interacts with at least partially dehydrated ions, is consistent with the observed lyotropic permeability sequence of certain isoforms[31,32]. The role of this subdomain in conferring a rate-limiting step for permeation[33] is reflected in the previously observed increase of outward rectification of currents after modification of a residue at the intracellular end of the VRAC selectivity filter with negatively charged MTS reagents[8]. The interaction of positively charged residues at the pore constriction with permeating anions is supported by the detectable sodium permeation and the decreased conductance of divalent anions of a mutant where the constricting arginine was removed (Fig. 6e, f, Extended Data Fig. 9g–n). The remaining preference for anions of the mutated channel is likely conferred by positively charged residues distributed along the pore (Figs. 4a, 6a, g, Extended Data Figs. 8f and 9g, h). Although our low-resolution data of mLRRC8A/C channels suggest a similar geometry of the constricted extracellular region compared to mLRRC8A (Fig. 1d, e, Extended Data Fig. 5c–f), it is currently unclear whether this structural unit is rigid or whether it changes its conformation during channel opening, closing or inactivation. In contrast to the anion selective channels composed of the LRRC8A and C subunits, VRAC heteromers containing the LRRC8D subunit display broader substrate specificity and allow permeation of diverse molecules including taurine, cisplatin and blasticidin[15-17]. In these channels, in which the constriction of D subunits contains a phenylalanine, the architecture of the filter might be altered to permit conduction of larger substrates. While the structure of the homomeric mLRRC8A is representative for the family,

its relation to a defined functional state and consequently the conformational changes of the channel upon activation are at this point ambiguous. The protein structure was determined at high salt concentration, a condition which in a cellular environment favors a closed conformation of VRACs[18]. The correspondence to a closed conformation is also consistent with the apparent shift in sensitivity of activation of the homomeric mLRRC8A construct towards lower ionic strength (Fig. 1c Extended Data Fig. 2h, i). However, apart from the constricted extracellular pore entrance and the unclear conformation of the N-terminus, the pore is wide and thus should allow the access of anions. In this respect, the role of the LRR domains and their potential structural rearrangement during activation are still unclear. Although interacting, these domains show a certain degree of flexibility as indicated by their poorly defined structure in sub-populations of the collected particles (Extended Data Fig. 3d). Moreover, due to the electrostatic nature of mutual interactions, their affinity could be influenced by the ion concentration and could thus contribute to channel activation during regulatory volume decrease (Fig. 5e). Still, the definitive location of the sensor of ionic strength and the mechanism of how conformational changes are coupled to pore opening are currently unknown. Other presently unclear features concern potential interaction partners of the LRR domains, the putative regulation by oxidative stress[34] and the role of phosphorylation of an intracellular loop[23,24] (Extended Data Fig. 1). These questions will have to be resolved in future studies for which the current data provides an important foundation.

1 Jentsch, T. J. VRACs and other ion channels and transporters in the regulation of cell volume and beyond. *Nat. Rev. Mol. Cell Biol.* **17**, 293-307 (2016).

2 Hoffmann, E. K., Lambert, I. H. & Pedersen, S. F. Physiology of cell volume regulation in vertebrates. *Physiol. Rev.* **89**, 193-277 (2009).

3 Okada, Y., Sato, K. & Numata, T. Pathophysiology and puzzles of the volume-sensitive outwardly rectifying anion channel. *J. Physiol.* **587**, 2141-2149 (2009).

4 Pasantes-Morales, H., Murray, R. A., Sanchez-Olea, R. & Moran, J. Regulatory volume decrease in cultured astrocytes. II. Permeability pathway to amino acids and polyols. *Am. J. Physiol.* **266**, C172-178 (1994).

5 Kimelberg, H. K., Goderie, S. K., Higman, S., Pang, S. & Waniewski, R. A. Swelling-induced release of glutamate, aspartate, and taurine from astrocyte cultures. *J. Neurosci.* **10**, 1583-1591 (1990).

6 Hyzinski-Garcia, M. C., Rudkouskaya, A. & Mongin, A. A. LRRC8A protein is indispensable for swelling-activated and ATP-induced release of excitatory amino acids in rat astrocytes. *J. Physiol.* **592**, 4855-4862 (2014).

7 Nilius, B. *et al.* Properties of volume-regulated anion channels in mammalian cells. *Prog. Biophys. Mol. Biol.* **68**, 69-119 (1997).

8 Qiu, Z. *et al.* SWELL1, a plasma membrane protein, is an essential component of volume-regulated anion channel. *Cell* **157**, 447-458 (2014).

9 Voss, F. K. *et al.* Identification of LRRC8 heteromers as an essential component of the volume-regulated anion channel VRAC. *Science* **344**, 634-638 (2014).

10 Sawada, A. *et al.* A congenital mutation of the novel gene LRRC8 causes agammaglobulinemia in humans. *J. Clin. Invest.* **112**, 1707-1713 (2003).

11 Kubota, K. *et al.* LRRC8 involved in B cell development belongs to a novel family of leucine-rich repeat proteins. *FEBS Lett.* **564**, 147-152 (2004).

12 Abascal, F. & Zardoya, R. LRRC8 proteins share a common ancestor with pannexins, and may form hexameric channels involved in cell-cell communication. *Bioessays* **34**, 551-560 (2012).

13 Bella, J., Hindle, K. L., McEwan, P. A. & Lovell, S. C. The leucine-rich repeat structure. *Cell. Mol. Life Sci.* **65**, 2307-2333 (2008).

14 Shimizu, T. Structural insights into ligand recognition and regulation of nucleic acid-sensing Toll-like receptors. *Curr. Opin. Struct. Biol.* **47**, 52-59 (2017).

15 Lee, C. C., Freinkman, E., Sabatini, D. M. & Ploegh, H. L. The protein synthesis inhibitor blasticidin s enters mammalian cells via leucine-rich repeat-containing protein 8D. *J. Biol. Chem.* **289**, 17124-17131 (2014).

16 Planells-Cases, R. *et al.* Subunit composition of VRAC channels determines substrate specificity and cellular resistance to Pt-based anti-cancer drugs. *Embo J* **34**, 2993-3008 (2015).

17 Lutter, D., Ullrich, F., Lueck, J. C., Kempa, S. & Jentsch, T. J. Selective transport of neurotransmitters and modulators by distinct volume-regulated LRRC8 anion channels. *J. Cell Sci.* **130**, 1122-1133 (2017).

18 Syeda, R. *et al.* LRRC8 Proteins Form Volume-Regulated Anion Channels that Sense Ionic Strength. *Cell* **164**, 499-511 (2016).

19 Nilius, B., Prenen, J., Voets, T., Eggermont, J. & Droogmans, G. Activation of volume-regulated chloride currents by reduction of intracellular ionic strength in bovine endothelial cells. *J. Physiol.* **506 (Pt 2)**, 353-361 (1998).

20 Maeda, S. *et al.* Structure of the connexin 26 gap junction channel at 3.5 A resolution. *Nature* **458**, 597-602 (2009).

21 Oshima, A., Tani, K. & Fujiyoshi, Y. Atomic structure of the innexin-6 gap junction channel determined by cryo-EM. *Nat. Commun.* **7**, 13681, doi:10.1038/ncomms13681 (2016).

22 Bennett, B. C. *et al.* An electrostatic mechanism for Ca(2+)-mediated regulation of gap junction channels. *Nat. Commun.* **7**, 8770, doi:10.1038/ncomms9770 (2016).

23 Huttlin, E. L. *et al.* A tissue-specific atlas of mouse protein phosphorylation and expression. *Cell* **143**, 1174-1189 (2010).

24 Zhou, H. *et al.* Toward a comprehensive characterization of a human cancer cell phosphoproteome. *J. Proteome Res.* **12**, 260-271 (2013).

25 Ullrich, F., Reincke, S. M., Voss, F. K., Stauber, T. & Jentsch, T. J. Inactivation and Anion Selectivity of Volume-regulated Anion Channels (VRACs) Depend on C-terminal Residues of the First Extracellular Loop. *J. Biol. Chem.* **291**, 17040-17048 (2016).

26 Sobolevsky, A. I., Rosconi, M. P. & Gouaux, E. X-ray structure, symmetry and mechanism of an AMPA-subtype glutamate receptor. *Nature* **462**, 745-756 (2009).

27 Matthies, D. *et al.* Cryo-EM Structures of the Magnesium Channel CorA Reveal Symmetry Break upon Gating. *Cell* **164**, 747-756 (2016).

28 Valiunas, V., Cohen, I. S. & Brink, P. R. Defining the factors that affect solute permeation of gap junction channels. *Biochim. Biophys. Acta* **1860**, 96-101 (2018).

29 Goldberg, G. S., Valiunas, V. & Brink, P. R. Selective permeability of gap junction channels. *Biochim. Biophys. Acta* **1662**, 96-101 (2004).

30 Nilius, B., Oike, M., Zahradnik, I. & Droogmans, G. Activation of a Cl- current by hypotonic volume increase in human endothelial cells. *J. Gen. Physiol.* **103**, 787-805 (1994).

31 Gaitan-Penas, H. *et al.* Investigation of LRRC8-Mediated Volume-Regulated Anion Currents in Xenopus Oocytes. *Biophys. J.* **111**, 1429-1443 (2016).

32 Pedersen, S. F., Okada, Y. & Nilius, B. Biophysics and Physiology of the Volume-Regulated Anion Channel (VRAC)/Volume-Sensitive Outwardly Rectifying Anion Channel (VSOR). *Pflugers Arch.* **468**, 371-383 (2016).

33 Paulino, C. *et al.* Structural basis for anion conduction in the calcium-activated chloride channel TMEM16A. *Elife* **6**, doi:10.7554/eLife.26232 (2017).

34 Gradogna, A., Gavazzo, P., Boccaccio, A. & Pusch, M. Subunit-dependent oxidative stress sensitivity of LRRC8 volume-regulated anion channels. *J. Physiol.* **595**, 6719-6733 (2017).

Supplementary Information is available in the online version of the paper.

Acknowledgements

This research was supported by a grant from the Swiss National Science Foundation (No. 31003A_163421). We thank O. Medalia and M. Eibauer, the Center for Microscopy and Image Analysis (ZMB) of the University of Zurich, and the Mäxi foundation for the support and access to the electron microscopes, S. Klauser and S. Rast for their help in establishing the computer infrastructure and T. J. Jentsch for providing the *LRRC8*$^{-/-}$ HEK cell-line. B. Blattmann and C. Stutz-Ducommun are acknowledged for help with crystallization screening of the

mLRRC8A^{LRRD} construct. X-ray data was collected at the X10SA Beamline at the Swiss Light Source of the Paul Scherrer Institute. Justin D. Walter is acknowledged for comments on the manuscript and all members of the Dutzler lab for their help at various stages of the project.

Author Contributions

D.D. generated expression constructs, purified proteins and determined the X-ray structure of the cytoplasmic domain. M.S. prepared the samples for cryo-EM, collected EM data and proceeded with structure determination. A.K.L recorded and analyzed electrophysiology data. C. P. established data processing infrastructure and performed initial screening of conditions for cryo-EM studies. D.D., M.S., A.K.L and R.D. jointly planned experiments, analyzed the data and wrote the manuscript.

Author Information

The authors declare no competing financial interests. Correspondence and requests for materials should be addressed to R.D. (dutzler@bioc.uzh.ch).

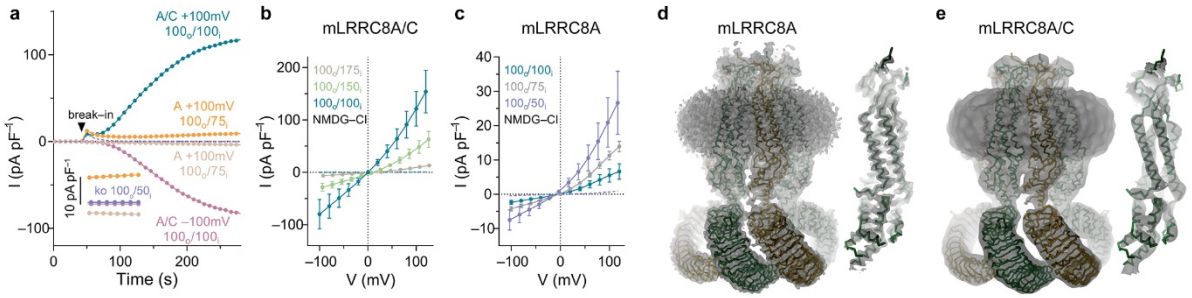

Figure 1 | Relationships between homomeric and heteromeric LRRC8 proteins. a, Whole-cell current response of *LRRC8*$^{-/-}$ cells expressing either mLRRC8A/C (cyan, pink) or mLRRC8A (orange, sand) upon a decrease of the intracellular ion concentration. Inset depicts a magnification of mLRRC8A currents during the plateau and endogenous currents (purple, magenta) from *LRRC8*$^{-/-}$ for comparison. Figure shows data from representative recordings at indicated ion concentrations. **b, c,** Current-voltage relationships of *LRRC8*$^{-/-}$ cells expressing mLRRC8A/C (**b**) and mLRRC8A (**c**) at different intracellular ion concentrations. Averages of four to seven independent experiments are shown, errors are SEM. **d, e,** Cryo-EM density of mLRRC8A at 4.25 Å (**d**) and mLRRC8A/C at 7.94 Å (**e**) superimposed on the refined model. Left, density of the entire channel contoured at 4σ. Right, Density around the TM domain of a single subunit contoured at 6.5σ.

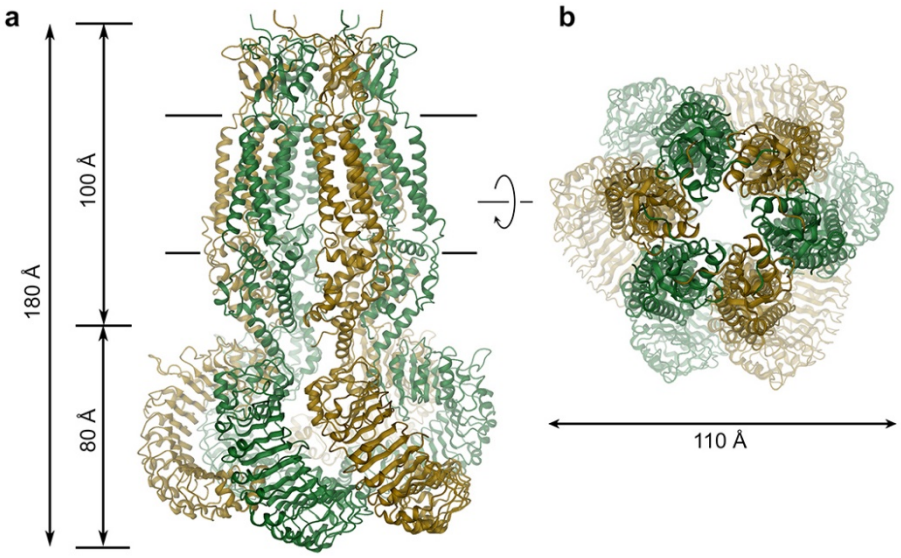

Figure 2 | LRRC8A structure. a, Ribbon representation of the hexameric mLRRC8A structure viewed from within the membrane. Membrane boundaries and molecular dimensions are indicated. **b,** mLRRC8A hexamer viewed from the extracellular side.

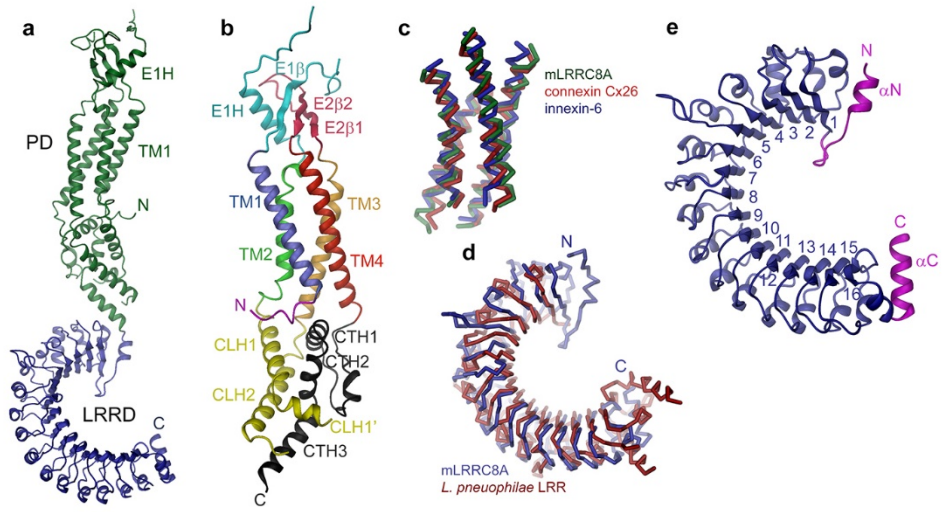

Figure 3 | LRRC8A subunit. a, Ribbon representation of the mLRRC8A subunit. PD and LRRD are colored in green and light blue, respectively. **b,** Structure of the PD with sections of the protein shown in unique colors and labeled. **c,** Superposition of the four transmembrane helices (as Cα-representation) of mLRRC8A with the equivalent regions of connexin Cx26 (PDBID: 2ZW3) and innexin-6 (PDBID: 5H1Q). **d,** Cα-representation of a superposition of the LRRD of mLRRC8A and the LRRD from *L. pneumophilae* (PDBID: 4Q62) **e,** Ribbon representation of the LRRD of mLRRC8A with selected secondary structure elements labeled.

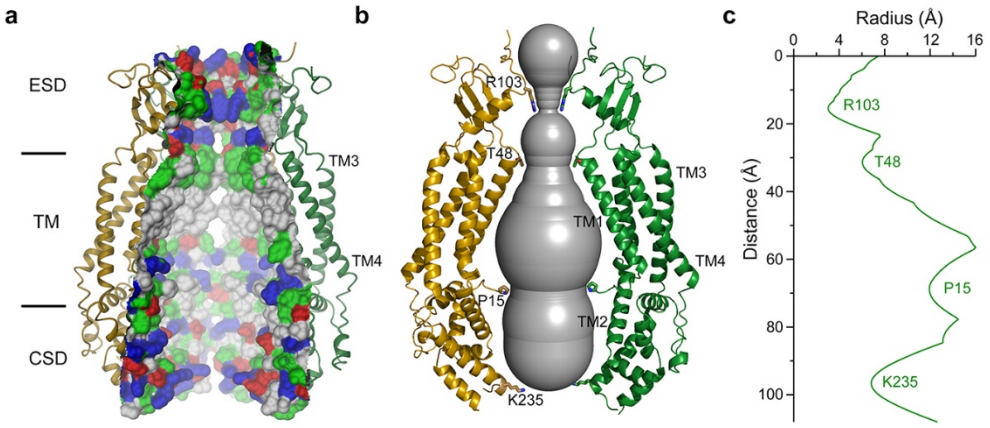

Figure 4 | Pore domain. a, Ribbon representation of the PD of mLRRC8A and molecular surface of the ion conduction path viewed from within the membrane. The two front subunits are removed for clarity. Surface is colored according to amino acid properties (green, polar; red, acidic; blue, basic). Sections of the PD are indicated. **b,** mLRRC8A pore displayed in relation to two opposite subunits with selected residues shown. **c,** Pore radius along the symmetry axis. Orientation and dimensions are as in **a**, **b**.

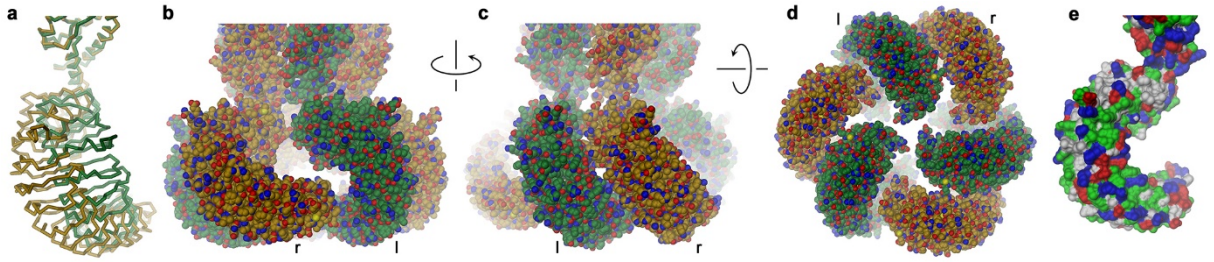

Figure 5 | Cytoplasmic LRR domains. a, Cα-trace of LRR domains of l (green) and r (orange) subunits after superposition of their PDs. **b-d**, View of the intracellular part of mLRRC8A. The protein is shown as space-filling model. The relationship between views is indicated. The view in c is as in Fig. 2a. **e,** Molecular surface of a single LRR domain with polar residues colored in green, basic residues in blue and acidic residues in red.

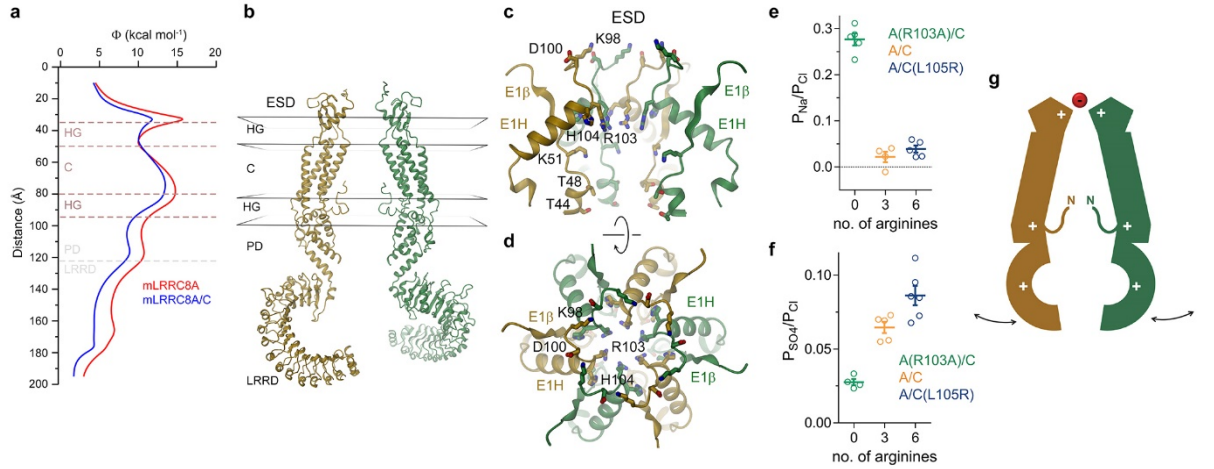

Figure 6 | Electrostatics and selectivity filter. a, Electrostatic potential along the pore of mLRRC8A (red) and a homology model of mLRRC8A/C (blue) as determined by a numerical solution of the Poisson-Boltzmann equation in the absence of mobile ions. Membrane boundaries (HG, lipid headgroups; C, hydrophobic core) and the border between PD and LRRD are indicated. **b**, Ribbon representation of two opposite subunits of the model used for electrostatics calculation in relation to the membrane (box). **c, d,** Part of the ESD lining the pore viewed from within the membrane with two front subunits removed for clarity (**c**) and from the extracellular side (**d**). The protein is displayed as ribbon and selected side chains as sticks. **e, f,** Cation/anion (**e**) and anion/anion (**f**) selectivity as a function of positive charge density in the selectivity filter (SF) recorded from the mutants mLRRC8A(R103A)/C (zero), mLRRC8A/C (assumed as three) and mLRRC8A/C(L105R) (six). Insets (top) show section of current-voltage relationships around the reversal potential. Data show mean of 4-6 independent experiments, errors are SEM. **g,** Schematic representation of the pore organization and electrostatics of a LRRC8 channel. A permeating anion is displayed as red sphere, movements of the cytoplasmic LRRDs potentially involved in activation are indicated.

METHODS

Expression constructs

The gene encoding mouse LRRC8A (NCBI: NP_808393.1) was codon-optimized for the expression in human cell lines (IDT) and synthesized by Genescript. The gene encoding mouse LRRC8C (NCBI: NP_598658.1) was acquired from OriGene. SapI restriction sites were removed by site-directed mutagenesis. All constructs were cloned into vectors that are based on pcDNA 3.1 (Invitrogen) and that were modified to be compatible with FX-cloning[35]. Unless stated otherwise, all fusion tags were located on the C-terminus and connected by a Rhinovirus 3C protease-cleavable linker. The construct containing only the pore domain of mLRRC8A (mLRRC8A^{PD}) consists of residues 1–428. The cytoplasmic domain construct of LRRC8A (mLRRC8A^{LRRD}) consists of residues 398–810. For expression of full-length mLRRC8A and mLRRC8A^{PD}, the protein was fused to mCherry followed by a myc-tag and streptavidin-binding peptide (SBP)[36]. For LRRC8A/LRRC8C co-expression mLRRC8A contained an mScarletI-His$_{10}$-tag[37] and mLRRC8C a Venus-myc-SBP tag. The cytosolic domain construct was fused N-terminally to Venus-myc-SBP. For electrophysiology all constructs were tagged with myc-SBP only.

Protein expression and purification

Suspension cultures of HEK293S GnTI^{-} cells[38] were grown in Pro293CDMs medium (Lonza) supplemented with 1% heat-inactivated FBS, 2 mM L-glutamine, 1 mM sodium pyruvate and 100 U ml^{-1} Penicillin-Streptomycin (Sigma) at 37 ºC and 5% CO_2. For protein expression cells were transiently transfected using a high-density transfection method with linear polyethylenimine (25 kDa, Polysciences) as described previously[39] with minor modifications. During the transfection step cells were resuspended in DMEM medium (with phenol red, 4,500 g l^{-1} glucose, Sigma). Plasmid DNA used for transfection was purified with a NucleoBond® Xtra Maxi kit (Machery-Nagel) from *E. coli* MC1061 cultures. HEK cells were harvested by centrifugation 36–48 h after transfection and washed with PBS. Pellets were flash-frozen in liquid nitrogen and stored at –20 °C for further use. The entire purification process was carried out at 4 °C. Full-length mLRRC8A and mLRRC8A^{PD} were purified as described below. 4–8 g of cell pellet from 1–2 l of suspension culture was resuspended in 40 ml of 25 mM Tris-HCl, pH 8.5, 250 mM NaCl, 3% digitonin (AppliChem) supplemented with 50 µg ml^{-1} DNAse (AppliChem), 50 µg ml^{-1} RNAse A (Sigma) and protease inhibitors (cOmplete EDTA-free, Roche). The mixture was incubated for 1.5 h under gentle agitation. Lysate was centrifuged for 30 min at 10,000 g and the supernatant was filtered through a 5 µm syringe filter (Minismart, Sartorius). Filtered supernatant containing the solubilized protein was mixed with 10 ml of StrepTactin Superflow resin (IBA Lifesciences) equilibrated with SEC buffer containing 25

mM Tris-HCl pH 8.5, 250 mM NaCl, 0.12% Digitonin (Calbiochem). The suspension was incubated in batch for 3 h under gentle agitation. The resin was subsequently washed with 250 ml of SEC buffer. The protein was eluted with 20 ml of SEC buffer supplemented with 15 mM D-desthiobiotin (Sigma) and incubated with 0.4 mg of 3C protease for 30 min to cleave the fusion tag. The sample was subsequently concentrated using a centrifugal filter (Amicon, 100 kDa MWCO), filtered (Millipore, 0.22 μm) and separated on a Superose 6 10/300 column (GE Healthcare) equilibrated in SEC buffer. Selected peak fractions containing the protein were pooled, concentrated and filtered. The analysis of the protein preparation my mass spectrometry revealed no significant contamination by endogenous LRRC8 subunits. For SEC-MALS experiments mLRRC8A^{PD} was purified as described above except that buffers contained 2% of n-Dodecyl-β-D-Maltoside (DDM, Anatrace) during extraction and 0.25 mM DDM in subsequent purification steps. Heteromeric mLRRC8A/C channels were expressed and purified in a similar way as described above with several modifications. The protein was purified from cells harvested from a 4 l culture (~20 g). After lysis, solubilization and centrifugation, the supernatant was supplemented with 5 mM imidazole and mixed with 10 ml of 6BCL-NTANi-500 resin (ABT) equilibrated with SEC buffer to purify channels containing the His_{10}-tagged mLRRC8A subunit. The suspension was incubated for 1 h under gentle agitation and resin containing bound protein was washed with 250 ml of SEC buffer supplemented with 5 mM imidazole. The protein was subsequently eluted with 30 ml of SEC buffer supplemented with 300 mM imidazole and loaded on a column containing 5 ml of Strep-Tactin Superflow resin (IBA) equilibrated with SEC buffer to bind channels containing the SBP-tagged mLRRC8C subunit. The Strep-Tactin resin was washed with 50 ml of SEC buffer and the protein was eluted with SEC buffer supplemented with 15 mM D-desthiobiotin (Sigma). Further purification and concentration proceeded as described for the homomeric mLRRC8A. The analysis of the preparation by mass spectrometry revealed similar ratios of A and C constructs and no significant contamination by endogenous subunits. The cytoplasmic domain construct mLRRC8A^{LRRD} was expressed in HEK293S GnTI^{-} cells and purified as described above with small modifications. The buffer used for extraction contained 10 mM Tris pH 9.4, 200 mM NaCl, 2% DDM, 50 μg $m1^{-1}$ DNAse (AppliChem) and protease inhibitors (cOmplete EDTA-free, Roche). After batch-binding of the protein, resin was washed with SEC2 buffer (10 mM Tris pH 9.4, 200 mM NaCl, 0.1% CHAPS). The protein was released from the resin by incubating the slurry with 0.8 mg 3C protease for 30 min. Eluted protein was concentrated (Amicon, 10 kDa) and separated on a Superdex 75 10/300 column (GE Healthcare) equilibrated with SEC2 buffer. Selected peak fractions were pooled. For crystallization, protein was concentrated (Amicon, 10 kDa MWCO) and supplemented with 0.5% CHAPS and 1 mM TCEP.

Molecular weight determination with SEC-MALS

Multi-angle light scattering experiments were performed at room temperature using an HPLC system (Agilent 1100) coupled to an Eclipse 3 system equipped with miniDAWN TREOS MALS detector and Optilab T-rEX refractometer (Wyatt Technology). 50 µl of purified $LRRC8A^{PD}$ protein, at a concentration of 1 mg ml^{-1} was separated on a Superose 6 10/300 Increase column against buffer containing 25 mM Tris-HCl pH 8.5, 250 mM NaCl and 0.25 mM DDM. The molecular weight was calculated with the Astra software (Astra 6.1, Wyatt Technologies) based on the absorption at 280 nm, light scattering, and the differential refractive index. Extinction coefficients at 280 nm (1.790 ml mg^{-1} cm^{-1}) and dn/dc values (0.190 mol ml g^{-2}) for $LRRC8A^{PD}$ were estimated using sedfit[40]. The dn/dc value for DDM was assumed as 0.133 mol ml g^{-2} (ref. 41).

Surface expression analysis

HEK 293 $LRRC8^{-/-}$ cells at 60 % confluency were transfected with 20 µg of DNA per 10-cm dish using Fugene 6 (Promega) and grown at 37 °C and 5% CO_2. Surface-expressed proteins were labeled with Sulfo-NHS-SS-Biotin 24 h post-transfection using the Pierce™ Cell Surface Protein Isolation Kit (Thermo Scientific™) according to manufacturer's protocol. Extraction and purification steps were carried out at 4°C. Cell pellet obtained from two 10-cm dishes was resuspended in 1 ml of PBS supplemented with 1% DDM, protease inhibitors, 10 µg ml^{-1} DNAse and 10 µg ml^{-1} RNAse A and incubated for 1 h under gentle agitation. Insoluble fractions were removed by centrifugation at 16,000 g for 30 min. The supernatant was mixed with 200 µl bed volume NeutrAvidin Agarose resin equilibrated with PBS and incubated for 2 h under gentle agitation. The flow-through was discarded and the resin was washed six times with 500 µl of PBS supplemented with 0.5 mM DDM. Captured proteins were eluted from the resin by incubation with SDS-PAGE loading buffer containing 50 mM fresh DTT for 1 h at 37 °C under vigorous mixing. Samples were separated by SDS-PAGE, transferred to a PVDF membrane and analyzed by Western-blotting using a mouse monoclonal anti-c-myc primary antibody (Sigma, M 4439**,** Clone 9E10) and goat anti-mouse-HRP conjugated secondary antibody (Jackson ImunoResearch, 115-035-146). The luminescent signal was developed with ECL substrate (Millipore) and recorded with a Fuji LAS3000 imaging system.

X-ray structure determination of the cytoplasmic LRR domain

The C-terminal domain construct $mLRRC8A^{LRRD}$ containing three additional residues on the N-terminus (Gly-Pro-Ser) and an additional Ala on the C-terminus was crystallized by vapor diffusion in sitting drops at 4 °C. Drops were prepared by mixing 0.1 µl of protein solution at a

concentration of 9.2 mg ml^{-1} with 0.1 µl of precipitant solution containing 0.1 M Bis-Tris propane pH 8.5, 0.2 M sodium malonate and 20% PEG3350 (NeXtal PACT Suite, Qiagen). Crystals were harvested after 3 weeks, cryo-protected in crystallization solution containing additional 30% of ethylene glycol and flash-frozen in liquid nitrogen. X-ray diffraction data were collected on the X10SA beamline at Swiss Light Source of the Paul-Scherrer Institute on a Pilatus 6M detector. Native and anomalous data (collected at a wavelength of 2.06 Å) were collected from the same crystal. Data were processed with XDS[42]. Crystals are of space group $P6_5$ and contain one copy of the molecule in their asymmetric unit. Initial phases were obtained by molecular replacement (MR) combined with single anomalous dispersion (SAD) with Phaser[43] implemented in the Phenix package[44] using anomalous data at a resolution of 2.5 Å. A partial search model for molecular replacement encompassing residues 644-755 of mLRRC8A was constructed from a homology model generated with I-TASSER[45] based on the crystal structure of a LRR domain protein (PDBID: 4U06, Chain A). An initial structure automatically built with Phenix AutoSol was used for molecular replacement against the native dataset (at a resolution of 1.8 Å). The complete structure was subsequently obtained by multiple iterations of structure building in Coot[46] and refinement with Phenix[44]. R_{free} was calculated based on 5% of reflections excluded from refinement. The final model consisting of 412 out of 416 residues, 300 waters and 10 ethylene glycols, is well-refined with R_{work} and R_{free} values of 20% and 21.3%, respectively. Unresolved residues include the N-terminal glycine and three residues (Gln-Ala-Ala) at the C-terminus.

Cryo-EM sample preparation and data collection

For structure determination of mLRRC8A by cryo-EM, 2.5 µl samples of purified protein at concentrations of 3.9–4.25 mg ml^{-1} were applied to glow-discharged holey carbon grids (Quantifoil R1.2/1.3 Au 200 mesh). For the structural characterization of the co-expressed mLRRC8A/C assembly, 2.5 µl samples at a protein concentration of 3.5 mg ml^{-1} were applied in a similar manner. Excess liquid was removed in a controlled environment (10 °C and 100% relative humidity) by blotting grids for 3–7 s (with a blotting force of 1 for mLRRC8A and 0 for mLRRC8A/C). Grids were subsequently flash frozen in liquid ethane using a Vitrobot Mark IV (Thermo Fisher Scientific). mLRRC8A (dataset 1) and mLRRC8A/C (dataset 3) were imaged in a 300 kV Tecnai G^2 Polara (FEI) with a 100 µm objective aperture. A second dataset of mLRRC8A (dataset 2) was recorded on a 300 kV Titan Krios (Thermo Fisher Scientific) with a 100 µm objective aperture. All data were collected using a post-column quantum energy filter (Gatan) with a 20 eV slit and a K2 Summit direct detector (Gatan) operating in super-resolution mode. Dose-fractionated micrographs were recorded in an automated manner using SerialEM[47] with a defocus range of –0.5 to –3.2 µm. Dataset 1 and dataset 3 was recorded at a nominal magnification of 37,313 corresponding to a pixel size of 1.34 Å/pixel (0.67 Å/pixel in super-resolution) with a total exposure time of 12.5 s (50 individual frames) and a dose of 1.4

$e^-/Å^2$/frame. Dataset 2 was recorded at a nominal magnification of 46,511 corresponding to a pixel size of 1.075 Å/pixel (0.5375 Å/pixel in super-resolution) with a total exposure time of 13 s (65 individual frames) and a dose of approximately 1.1 $e^-/Å^2$/frame. The total electron dose on the specimen level for all datasets was approximately 70 $e^-/Å^2$.

Cryo-EM image processing

Two independent datasets of mLRRC8A consisting of 9,209 (dataset 1) and 3,023 (dataset 2) micrographs were collected. The dataset of mLRRC8A/C consisted of 1,545 micrographs (dataset 3). The recorded super-resolution images were down-sampled twice by Fourier cropping and all individual frames were used for correction of beam-induced movement using a dose-weighting scheme in MotionCor2 (ref. 48). The CTF parameters were estimated on movie frames using CTFFIND4 (ref. 49). Low-quality micrographs showing a significant drift, high defocus or poor CTF estimates were discarded resulting in datasets of 6,231 images for the mLRRC8A Polara dataset, 1,817 images for the mLRRC8A Titan Krios dataset and 1,127 images of the mLRRC8A/C dataset, which were subjected to further data processing using RELION2.1b1[50,51]. From the mLRRC8A Polara dataset, 8,208 particles were extracted with a box size of 344 pixels and subjected to an initial reference-free 2D classification. From this set, five distinctive 2D class averages were selected and used as templates for automated particle picking, which generated a starting dataset of 329,624 particles. False positives and particles of poor quality were discarded through a round of 2D classification decreasing the number of particles to 287,953. The initial 3D reconstruction, which was generated in RELION from 3,600 randomly chosen cleaned particles, was low-pass filtered to 60 Å and used as a template in a subsequent 3D classification. Independent rounds of 3D classification with a different number of classes were performed in order to isolate the most homogeneous subset of particles. Out of nine classes, one revealed a fully assembled reconstruction with a clear indication of a global C3 symmetry. 54,861 particles belonging to this class were subjected to auto-refinement with imposed C3 symmetry and particle polishing with a running average window of 7, a standard deviation of 1 pixel on translations and 400 pixels on particle distance. The final map was auto-refined to 5.01 Å in the presence of a soft solvent mask and sharpened using an isotropic b-factor of –173 $Å^2$. This map was then low-pass filtered to 60 Å and used as a 3D reference for processing of the mLRRC8A dataset collected on a Titan Krios. 105,867 particles were picked automatically using seven representative 2D class averages from the Polara dataset and subsequently subjected to 3D classification. The initial clean-up of the starting pool of particles through 2D classification was deliberately omitted in order not to discard any particles representing underpopulated views. Similarly to the Polara dataset, independent rounds of 3D classification were performed to identify the most homogeneous subset of particles. Out of five classes, one has shown the same conformation with a clear three-fold symmetry in the cytoplasmic LRR domain and a six-fold symmetry in the transmembrane domain, as observed previously for the Polara dataset. 34,674 particles belonging to this class were polished with a

running average window of 7, a standard deviation of 1 pixel on translations and 500 pixels on particle distance. The resulted class was auto-refined to 4.25 Å and sharpened using an isotropic b-factor of –118 Å^2. Despite the increase in the overall resolution, as compared to the map generated from the Polara dataset, the map from the Titan dataset showed considerably weaker density in the cytoplasmic domain, indicating its intrinsic flexibility. In order to improve the density of the transmembrane domain a focused 3D refinement with partial signal subtraction was performed[52]. In this approach, the density corresponding to the cytoplasmic domain was subtracted from the original particles. *In silico* modified particles (dataset 2a) were subsequently subjected to auto-refinement with C6 symmetry imposed in the presence of a soft mask around the transmembrane domain. The final map at 3.66 Å was sharpened using an isotropic b-factor of –96 Å^2. The initial dataset of mLRRC8A/C contained 101,239 particles, which were subjected to 2D classification in order to discard broken particles, small aggregates and to assess sample heterogeneity. Due to the increased flexibility in the LRR domains of heteromeric complexes, 3D refinement was performed by either imposing no or C3 symmetry on 94,369 particles selected after 2D classification. Euler angles of the best matching reference to each particle from the cleaned dataset 3 were assigned using a 40 Å low-pass filtered model (obtained from dataset 1) as an initial template. Particles, which were assigned incorrect orientations, were discarded through another round of 2D classification, where the alignment step was deliberately omitted. In order to segregate the remaining structural heterogeneity, particles were subjected to a side-by-side non-symmetrized and C3-symmetrized 3D classification. In the non-symmetrized case, the two highest ranking classes were selected and 59,315 particles were auto-refined imposing C3 symmetry to yield a reconstruction of 8.23 Å. For C3 symmetrized classification, the best class contained 27,777 particles and was auto-refined with C3 symmetry to yield a reconstruction at 7.94 Å. In all cases resolution was estimated in the presence of a soft solvent mask and based on the gold standard Fourier Shell Correlation (FSC) 0.143 criterion[50,53-55]. High-resolution noise substitution was applied to correct FSC curves for the effect of soft masking in real space[53]. The local resolution was estimated using BlocRes from the Bsoft package[56,57].

Model building and Refinement

The model of the transmembrane domain of mLRRC8A was built in Coot[46]. The cryo-EM density of the transmembrane region generated from focused refinement applying C6 symmetry was of high quality and allowed the unambiguous assignment of residues 15–68, 92–176 and 230–408. As reflected by the variations in local resolution, the density of the terminal helix connecting to the cytoplasmic LRR domain, was less well-defined than the density of the pore and other intra- and extracellular regions. The model was improved iteratively by cycles of real-space refinement in PHENIX[44] with secondary structure and 6-fold NCS constraints applied, reciprocal-space refinement in REFMAC5[58,59] and manual corrections in Coot. The model of

full-length mLRRC8A was assembled from the transmembrane and cytoplasmic domains fitted into the 4.25 Å electron density of the C3 symmetrized hexamer using UCSF Chimera[60]. The structure of the LRRD in our cryo-EM reconstruction of the full-length channel is essentially unaltered compared to the X-ray structure and the connection between PD and LRRD is unambiguously defined by the overlapping α-helix CTH3, which is present in both structures. Both domains were initially defined as independent entities and refined as rigid bodies. In a later stage, the PD and LRRD were linked into a single polypeptide chain and refinement proceeded as described above maintaining tree-fold NCS and secondary structure constraints. Validation of the refinement of the transmembrane and the full-length models was performed in REFMAC5, distributed as part of the CCP-EM suite[61], and represented as Fourier Shell Correlations (FSC_{sum}) between the refined models and their corresponding final cryo-EM density maps. For cross-validation the cryo-EM dataset was split into two subsets which were used to calculate two independent maps (half map 1 and half map 2). To detect possible overfitting and hence over-estimation of the resolution, random shifts, up to 0.5 Å, were applied to the coordinates of each model, which was then refined against the unfiltered half map 1. The cross-validation was done by comparing the FSC_{work} (estimated for the shaken-refined model and half map 1) and the FSC_{free} (estimated for the shaken-refined model and half map 2, which was not used in the refinement). Pore dimensions were calculated with HOLE[62] and surfaces with MSMS[63]. Figures and movies containing molecular structures and densities were prepared with DINO (http://www.dino3d.org), Pymol[64] and Chimera[60].

Modeling and Poisson-Boltzmann calculations

The homology model of the mLRRC8C subunit was prepared with the SWISS-MODEL homology modelling server[65]. Regions not defined in the cryo-EM density of mLRRC8A were excluded from the model, except for the N-terminal 14 amino acids that were modelled into both, the homomeric mLRRC8A structure and the heteromeric mLRRC8A/C structure consisting of alternating A and C subunits used for electrostatic calculations. The electrostatic potential of the m mLRRC8A and the m mLRRC8A/C hexamers was calculated by solving the linearized Poisson–Boltzmann equation in CHARMM[66,67] on a 240 Å × 240 Å × 260 Å grid (1 Å grid spacing) followed by focusing on a 160 Å x 160 Å x 200 Å grid (0.5 Å grid spacing). Partial protein charges were derived from the CHARMM36 all-hydrogen atom force field. Hydrogen positions were generated in CHARMM. Histidines were deprotonated. The protein was assigned a dielectric constant (ϵ) of 2. Its transmembrane region was embedded in a 30 Å-thick slab (ϵ = 2) representing the hydrophobic core of the membrane and two adjacent 15 Å-thick regions (ϵ = 30) representing the headgroups. The membrane region contained a 60 Å-high and 20 Å-wide aqueous cylinder (ϵ = 80) around the VRAC pore and was surrounded by an aqueous environment (ϵ = 80). Calculations were carried out in either 0 or 150 mM of monovalent mobile ions in the aqueous regions.

Electrophysiology

LRRC8$^{-/-}$ HEK293 cells (kindly provided by T. J. Jentsch) were transfected with the constructs of interest at 3 μg total DNA per 6-cm Petri dish using the calcium phosphate co-precipitation method. mLRRC8 constructs not containing fluorescent protein tags were co-transfected with a Venus-only construct, at an mLRRC8:Venus ratio of 2:1, to aid identification of transfected cells. Cells were used the day after transfection. mLRRC8 constructs were transfected at a 1:1 ratio. Whole-cell patch-clamp was performed on single *LRRC8*$^{-/-}$ HEK293 cells expressing the mLRRC8 constructs of interest. Seal resistance was typically 4 GΩ or higher before the establishment of the whole-cell configuration. Patch pipettes were pulled from borosilicate glass capillaries with an outer diameter of 1.5 mm and inner diameter of 0.86 mm (Sutter) and were fire-polished before use. Pipette resistance was typically 6–12 MΩ when filled with the iso-osmotic low ionic strength solution (see below) required to activate the LRRC8 channel. Series resistance was compensated by 60–80% and was typically between 2–8 MΩ after compensation. Voltage-clamp recordings were performed using Axopatch 200B and Digidata 1550 (Molecular devices). Analogue signals were filtered at 5 kHz using the in-built 4-pole Bessel filter and were digitized at 10–20 kHz. Data acquisition was performed using Clampex 10.6 (Molecular devices). Local perfusion was achieved using a gravity-fed system through a double-barreled theta glass pipette. Liquid junction potential, calculated in Clampex, was corrected when it is larger than 2 mV. All experiments were performed at 20 °C. All recording solutions used in this study were approximately iso-osmotic with an osmolality of 308–330 mmol kg^{-1} as measured using a vapor pressure osmometer (VAPRO®). The solutions were also designed to create a minimal junction potential (less than 2 mV) when used as local perfusates. Unless otherwise indicated, recordings were performed under symmetrical ionic conditions. For anion permeability experiments, bi-ionic conditions were used. Pipette solution with a standard sub-physiological ionic strength contained 100 mM NMDG-Cl, 100 mM D-mannitol, 1 mM EGTA, 3 mM Na_2ATP and 10 mM HEPES at pH 7.40. When lower ionic strength was required, the salt/mannitol ratio were adjusted accordingly to maintain an approximately equal osmolarity. Extracellular solution contained 100 mM NMDG-Cl, 100 mM D-mannitol, 1.99 mM $Ca(OH)_2$, 1 mM EGTA and 10 mM HEPES at pH 7.40. When SO_4^{2-} was used as a charge carrier, the extracellular solution contained 100 mM $(NMDG)_2SO_4$, 1.99 mM $Ca(OH)_2$, 1 mM EGTA and 10 mM HEPES at pH 7.40. In cation permeability experiments, the extracellular solution contained 150 mM NaCl, 1.99 mM $Ca(OH)_2$, 1 mM EGTA and 10 mM HEPES at pH 7.40. The use of these solutions allowed us to record LRRC8-mediated currents with defined ionic composition on both the extracellular and intracellular sides with minimal interference by osmosis. This is crucial for the rigorous examination and interpretation of both activation and current-voltage characteristics of LRRC8 channels. Activation of LRRC8 proteins by iso-osmotic pipette solutions with sub-physiological ionic strength was monitored using a ramp

protocol delivered every 2–4 seconds. Conduction and permeation characteristics of LRRC8 proteins were examined through their current-voltage (I-V) relationships constructed from instantaneous current responses following a voltage jump in a step protocol from –100 mV to +120 mV with a 20 mV increment per step. Instantaneous I-V relationships were corrected for activity changes during the step protocol by normalizing to the current amplitudes during a –40 mV pre-pulse. Membrane potential was held close to the Nernst potential of Cl^- when Cl^- was the only charge carrier or the reversal potential when bi-ionic or asymmetrical conditions were used to minimize asymmetrical changes of ion concentration in the extracellular and intracellular compartments. Relative permeability for monovalent cation was calculated using

$$\frac{P_{Na}}{P_{Cl}} = \frac{[Cl^-]_o e^{\frac{FE_{rev}}{RT}} - [Cl^-]_i}{[Na^+]_o}$$

and that for divalent anion was calculated using

$$\frac{P_{SO4}}{P_{Cl}} = \frac{[Cl^-]_i}{4[{SO_4}^{2-}]_o}(1 + e^{-\frac{FE_{rev}}{RT}})e^{-\frac{FE_{rev}}{RT}}$$

where E_{rev} is the reversal potential, $\frac{P_X}{P_{Cl}}$ is the permeability of the ionic species of interest relative to that of Cl^-, and R, T and F have their usual meanings. Data were analyzed using Clampfit 10.6 (Molecular devices), Excel (Microsoft) and Prism 5 or 6 (GraphPad), and are presented as mean ± SEM.

Statistics and Reproducibility

Electrophysiology data were repeated multiple times from different transfections with very similar results. Conclusions of experiments were not changed upon inclusion of further data. In all cases, leaky patches were discarded.

Data availability

The three-dimensional cryo-EM density maps have been deposited in the Electron Microscopy Data Bank under accession numbers EMD-4366, EMD-4367, EMD-4362 and EMD-4361, respectively. The deposition includes corresponding maps calculated with higher b-factors, both half-maps, and the mask used for final FSC calculation. Coordinates for the models of mLRRC8A, the mLRRC8A pore domain and the mLRRC8A LRR domain have been deposited in the Protein Data Bank under accession numbers 6G9L, 6G9O, 6G8Z and 6FNW respectively. Data can be made available upon reasonable request.

35 Geertsma, E. R. & Dutzler, R. A versatile and efficient high-throughput cloning tool for structural biology. *Biochemistry* **50**, 3272-3278 (2011).

36 Keefe, A. D., Wilson, D. S., Seelig, B. & Szostak, J. W. One-step purification of recombinant proteins using a nanomolar-affinity streptavidin-binding peptide, the SBP-Tag. *Prot. Expr. Purif.* **23**, 440-446 (2001).

37 Bindels, D. S. *et al.* mScarlet: a bright monomeric red fluorescent protein for cellular imaging. *Nat. Methods* **14**, 53-56 (2017).

38 Reeves, P. J., Callewaert, N., Contreras, R. & Khorana, H. G. Structure and function in rhodopsin: high-level expression of rhodopsin with restricted and homogeneous N-glycosylation by a tetracycline-inducible N-acetylglucosaminyltransferase I-negative HEK293S stable mammalian cell line. *Proc. Natl. Acad. Sci. USA* **99**, 13419-13424 (2002).

39 Hacker, D. L. *et al.* Polyethyleneimine-based transient gene expression processes for suspension-adapted HEK-293E and CHO-DG44 cells. *Prot. Expr. Purif.* **92**, 67-76 (2013).

40 Schuck, P. Size-distribution analysis of macromolecules by sedimentation velocity ultracentrifugation and lamm equation modeling. *Biophys. J.* **78**, 1606-1619 (2000).

41 Strop, P. & Brunger, A. T. Refractive index-based determination of detergent concentration and its application to the study of membrane proteins. *Protein. Sci.* **14**, 2207-2211 (2005).

42 Kabsch, W. Automatic Processing of Rotation Diffraction Data from Crystals of Initially Unknown Symmetry and Cell Constants. *J. Appl. Crystallogr.* **26**, 795-800 (1993).

43 McCoy, A. J. *et al.* Phaser crystallographic software. *J. Appl. Crystallogr.* **40**, 658-674 (2007).

44 Adams, P. D. *et al.* PHENIX: building new software for automated crystallographic structure determination. *Acta Crystallogr. D Biol. Crystallogr.* **58**, 1948-1954 (2002).

45 Yang, J. *et al.* The I-TASSER Suite: protein structure and function prediction. *Nat. Methods* **12**, 7-8 (2015).

46 Emsley, P. & Cowtan, K. Coot: model-building tools for molecular graphics. *Acta Crystallogr. D Biol. Crystallogr.* **60**, 2126-2132 (2004).

47 Mastronarde, D. N. Automated electron microscope tomography using robust prediction of specimen movements. *J. Struct. Biol.* **152**, 36-51 (2005).

48 Zheng, S. Q. *et al.* MotionCor2: anisotropic correction of beam-induced motion for improved cryo-electron microscopy. *Nat. Methods* **14**, 331-332 (2017).

49 Rohou, A. & Grigorieff, N. CTFFIND4: Fast and accurate defocus estimation from electron micrographs. *J. Struct. Biol.* **192**, 216-221 (2015).

50 Scheres, S. H. RELION: implementation of a Bayesian approach to cryo-EM structure determination. *J. Struct. Biol.* **180**, 519-530 (2012).

51 Kimanius, D., Forsberg, B. O., Scheres, S. H. & Lindahl, E. Accelerated cryo-EM structure determination with parallelisation using GPUs in RELION-2. *Elife* **5**, doi:10.7554/eLife.18722 (2016).

52 Bai, X. C., Rajendra, E., Yang, G., Shi, Y. & Scheres, S. H. Sampling the conformational space of the catalytic subunit of human gamma-secretase. *Elife* **4**, doi:10.7554/eLife.11182 (2015).

53 Chen, S. *et al.* High-resolution noise substitution to measure overfitting and validate resolution in 3D structure determination by single particle electron cryomicroscopy. *Ultramicroscopy* **135**, 24-35 (2013).

54 Rosenthal, P. B. & Henderson, R. Optimal determination of particle orientation, absolute hand, and contrast loss in single-particle electron cryomicroscopy. *J. Mol. Biol.* **333**, 721-745 (2003).

55 Scheres, S. H. & Chen, S. Prevention of overfitting in cryo-EM structure determination. *Nat. Methods* **9**, 853-854 (2012).

56 Heymann, J. B. & Belnap, D. M. Bsoft: image processing and molecular modeling for electron microscopy. *J. Struct. Biol.* **157**, 3-18 (2007).

57 Cardone, G., Heymann, J. B. & Steven, A. C. One number does not fit all: mapping local variations in resolution in cryo-EM reconstructions. *J. Struct. Biol.* **184**, 226-236 (2013).

58 Murshudov, G. N. *et al.* REFMAC5 for the refinement of macromolecular crystal structures. *Acta Crystallogr. D Biol. Crystallogr.* **67**, 355-367 (2011).

59 Brown, A. *et al.* Tools for macromolecular model building and refinement into electron cryo-microscopy reconstructions. *Acta Crystallogr. D Biol. Crystallogr.* **71**, 136-153 (2015).

60 Pettersen, E. F. *et al.* UCSF Chimera--a visualization system for exploratory research and analysis. *J. Comput. Chem.* **25**, 1605-1612 (2004).

61 Burnley, T., Palmer, C. M. & Winn, M. Recent developments in the CCP-EM software suite. *Acta Crystallogr. D Struct. Biol.* **73**, 469-477 (2017).

62 Smart, O. S., Neduvelil, J. G., Wang, X., Wallace, B. A. & Sansom, M. S. HOLE: a program for the analysis of the pore dimensions of ion channel structural models. *J. Mol. Graph.* **14**, 354-360 (1996).

63 Sanner, M. F., Olson, A. J. & Spehner, J. C. Reduced surface: an efficient way to compute molecular surfaces. *Biopolymers* **38**, 305-320 (1996).

64 DeLano, W. L. Pymol: An open-source molecular graphics tool. *CCP4 Newsletter On Protein Crystallography* **40**, 82-92 (2002).

65 Biasini, M. *et al.* SWISS-MODEL: modelling protein tertiary and quaternary structure using evolutionary information. *Nucleic Acids Res.* **42**, W252-258 (2014).

66 Brooks, B. R. *et al.* CHARMM: a program for macromolecular energy, minimization, and dynamics calculations. *J. Comp. Chem.* **4**, 187-217 (1983).

67 Im, W., Beglov, D. & Roux, B. Continuum solvation model: Electrostatic forces from numerical solutions to the Poisson-Bolztmann equation. *Comput. Phys. Commun.* **111**, 59-75 (1998).

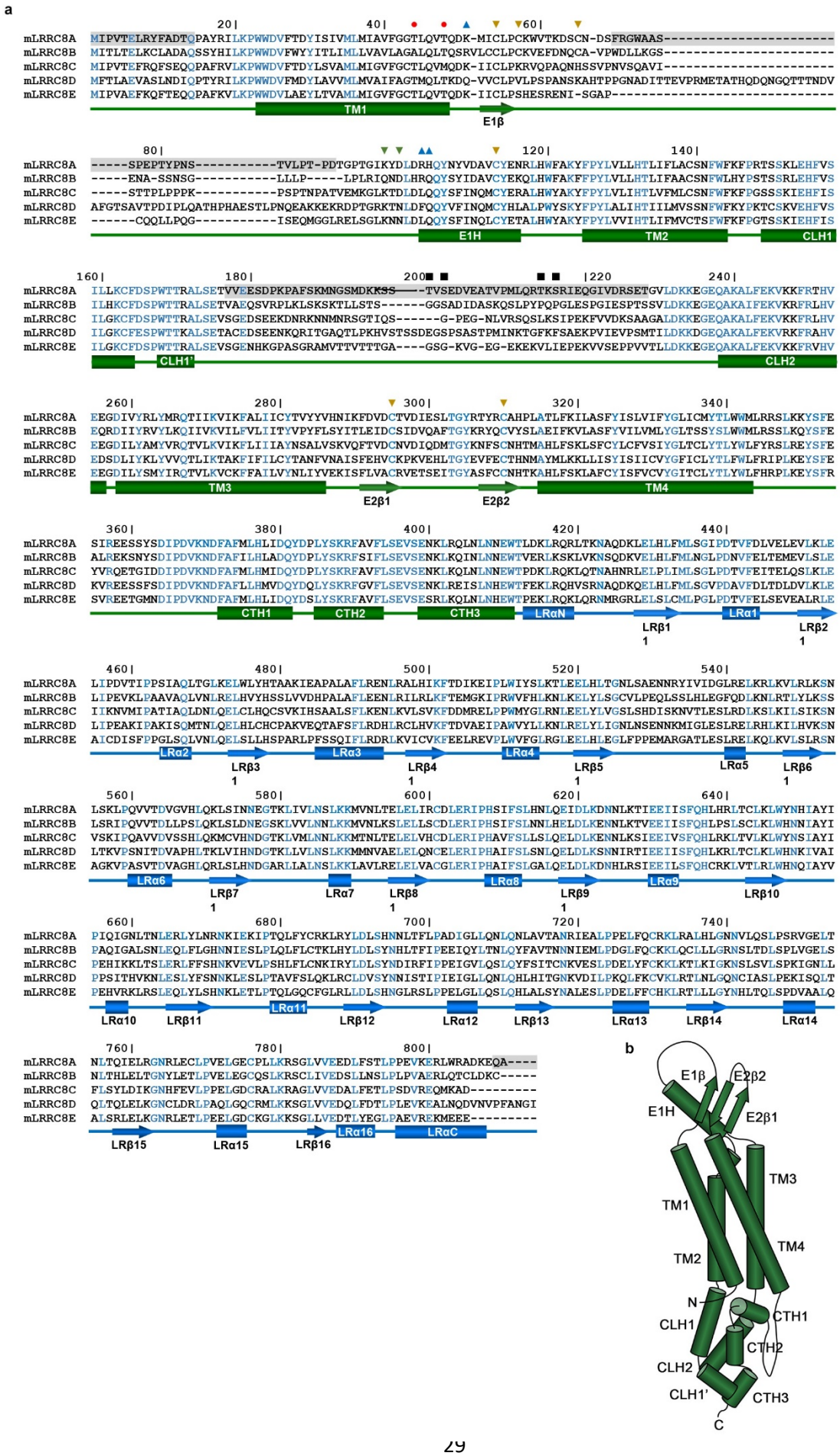
a
mLRRC8A
mLRRC8B
mLRRC8C
mLRRC8D
mLRRC8E
TM1
E1β
E1H
TM2
CLH1
CLH1'
CLH2
TM3
E2β1
E2β2
TM4
CTH1
CTH2
CTH3
LRαN
LRβ1
LRα1
LRβ2
LRα2
LRβ3
LRα3
LRβ4
LRα4
LRβ5
LRα5
LRβ6
LRβ7
LRα7
LRβ8
LRα8
LRβ9
LRα9
LRβ10
LRα6
LRα10
LRβ11
LRα11
LRβ12
LRα12
LRβ13
LRα13
LRβ14
LRα14
LRβ15
LRα15
LRβ16
LRα16
LRαC
b
E1β
E2β2
E1H
E2β1
TM3
TM1
TM4
TM2
N
CLH1
CTH1
CTH2
CLH2
CLH1'
CTH3
C

Extended Data Figure 1 | Sequence alignment and topology. a, Multiple sequence alignment of mouse paralogues of LRRC8. Shown are the sequences of mLRRC8A (NCBI: NP_808393), mLRRC8B (NCBI: NP_001028722), mLRRC8C (NCBI: NP_598658), mLRRC8D (NCBI: NP_001116240) and mLRRC8E (NCBI: NP_082451). Residues strictly conserved in all subunits are colored in blue. Segments of mLRRC8A that are not defined in the cryo-EM density are highlighted in grey. Secondary structure elements of mLRRC8A are shown below (green PD, light blue LRRD). Numbering corresponds to mLRRC8A. Red spheres, two threonine residues facing the pore at the extracellular membrane boundary; blue triangles, basic residues of the ESD of mLRRC8A facing the pore; yellow inverted triangles, cysteine residues involved in disulfide bridges; green inverted triangles, residues at the extracellular side that play a role in desensitization; black squares, annotated phosphorylation sites (Uniprot: Q80WG5). The two paralogs mLRRC8A and C investigated in this study are of similar length and share 58% of identical and 72% of homologous residues. **b,** Topology of the PD with secondary structure elements indicated.

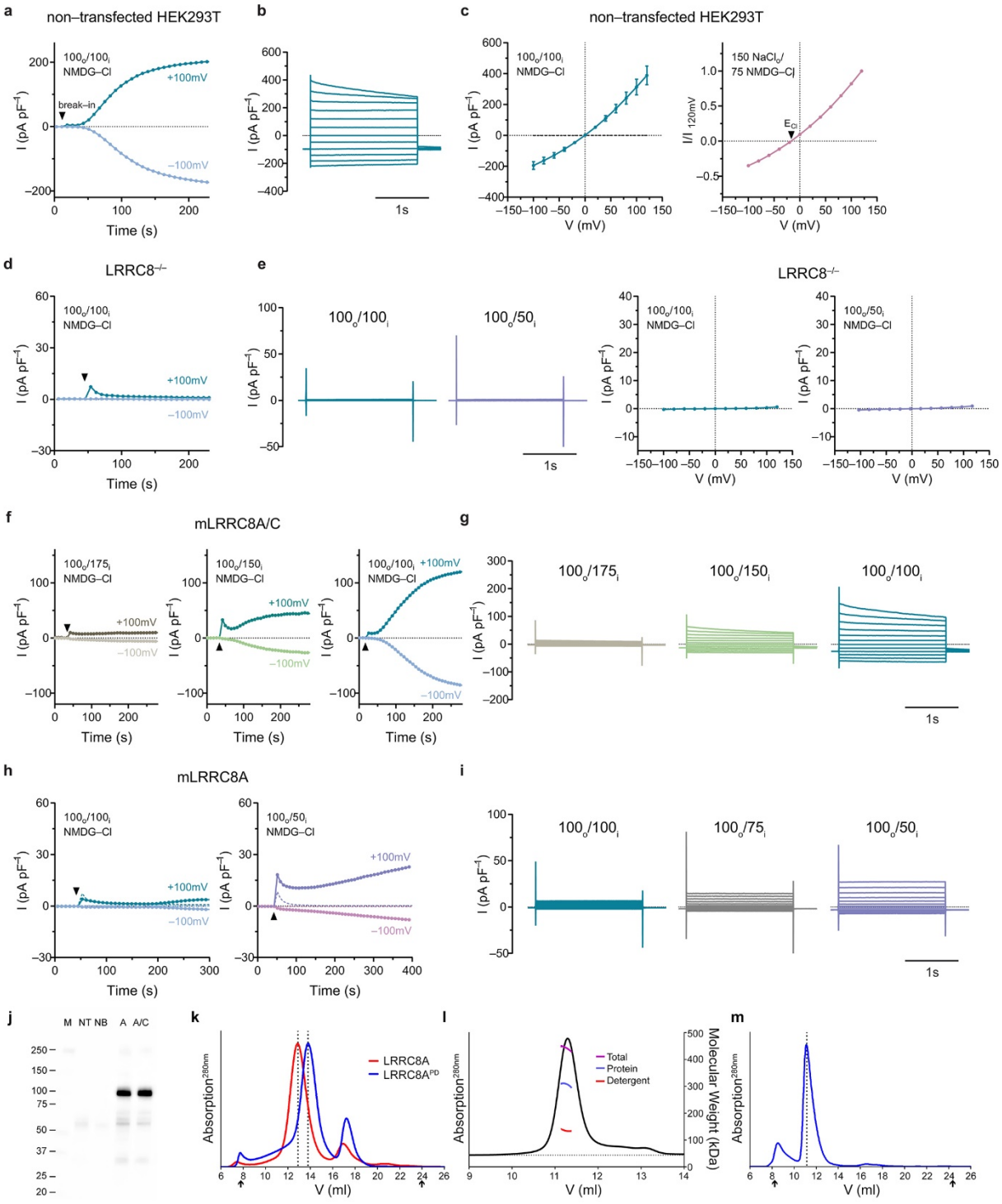

Extended Data Figure 2 | Electrophysiology and biochemical characterization. a, Time-dependent whole-cell currents of non-transfected HEK293T cells recorded at 100 mV (dark blue) and –100 mV (light blue) evoked in response to low intracellular ion concentration (100 mM NMDG-Cl). **b,** Representative current response of activated channels at different voltages at symmetric 100 mM Cl^- concentration. **c,** Current-voltage relationships in symmetric (left) and asymmetric ionic conditions (right). The negative reversal potential in asymmetric conditions is indicative for an anion selective channel. **d,** Time-dependent response and **e,** representative traces

and current-voltage relationships of the LRRC8 knock-out cell-line *LRRC8*$^{-/-}$ at the indicated ion concentrations. **f,** Time-dependent response and **g,** current response of *LRRC8*$^{-/-}$ cells expressing mLRRC8A/C at the indicated ion concentrations. **h,** Time-dependent response and **i,** current response of *LRRC8*$^{-/-}$ cells expressing mLRRC8A at the indicated ion concentrations. Dashed lines show the corresponding responses of *LRRC8-/-* cells at the indicated ion concentrations. Data in **a–i** were recorded under voltage-clamp conditions in the whole-cell configuration. **b**, **e, g, i,** Traces show representative data recorded during the plateau at the indicated Cl^- concentrations. Current-voltage relationships show averages of four to seven independent experiments, errors are SEM. **a, d, f, h,** the black triangle indicates the point of break-in. **j**, Plasma membrane expression of LRRC8 constructs probed by surface biotinylation. Western blot showing avidin-purified chemically biotinylated proteins at the cell surface, which are detected by an anti-myc antibody recognizing a fusion tag on overexpressed mLRRC8 construct. Lanes show M, marker with molecular weights indicated; NT, non-transfected biotinylated HEK293 LRRC8-/- (ko) cells; NB, mLRRC8A/C transfected, non-biotinylated ko cells; A, mLRRC8A transfected, biotinylated ko cells; AC, mLRRC8A/C transfected, biotinylated ko cells; C, mLRRC8C transfected, biotinylated ko cells. The blot shows similar surface expression of mLRRC8A and mLRRC8A/C constructs, whereas mLRRC8C constructs are poorly targeted to the plasma membrane, which is in agreement with previous reports[2]. **k,** Elution profile of mLRRC8A (red) and mLRRC8A^{PD} (blue) from a Superose 6 10/300 column. The first peak between 13–14 ml corresponds to a hexamer of mLRRC8A, the smaller peak around 17 ml to the cleaved fluorescent fusion protein. **l,** Elution profile and derived molecular weight for mLRRC8A^{PD} purified in DDM. The continuous black line shows normalized absorbance at 280nm. The calculated molecular weight of the entire complex and its protein and detergent components based on MALS experiments are shown in purple, blue and red respectively. The calculated values are consistent with a hexameric assembly of mLRRC8A^{PD}. **m**, Elution profile of mLRRC8A^{LRRD} from a Superdex 75 10/300 column. The main peak around 12 ml corresponds to a monomer of the cytoplasmic domain. **k, m,** Arrows indicate the void and bed volume.

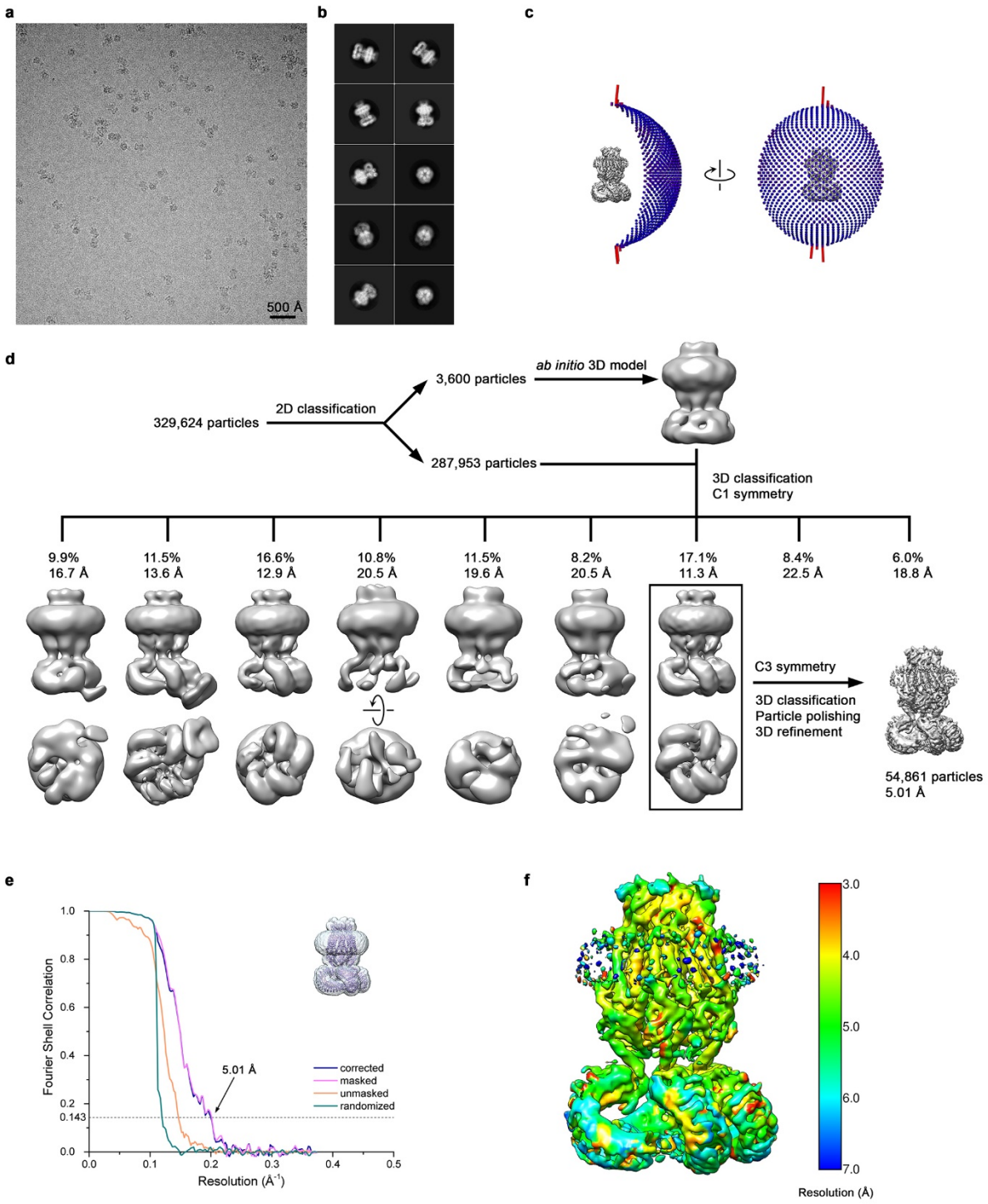

Extended Data Figure 3 | Cryo-EM reconstruction of mLRRC8A at 5.01 Å. a, Representative cryo-EM micrograph of dataset 1 acquired with a FEI Tecnai G^2 Polara microscope. The image shows well-dispersed single particles with occasional micro-aggregates. **b,** 2D class averages of mLRRC8A and **c,** angular distribution plot of all particles included in the final C3-symmetrized reconstruction show uniform orientations. The length and the color of cylinders correspond to the number of particles with respective Euler angles. **d,** Data processing workflow. Seven out of nine classes generated during 3D classification reveal a well-defined, C6-symmetric PD and structural heterogeneity in the LRRDs reflecting their intrinsic mobility. The second class from the left shows additional density representing a part of the cytoplasmic subunits of a neighboring particle. Particles assigned to the boxed

class were used in further refinement. The distribution of all particles (%) and the resolution of each class is indicated. **e,** Fourier Shell Correlation (FSC) plot of the final refined unmasked (orange), masked (pink), phase-randomized (green) and corrected for mask convolution effects (blue) cryo-EM density map of mLRRC8A. The resolution at which the FSC curve drops below the 0.143 threshold is indicated. Inset shows the atomic model within the mask that was applied for calculations of the resolution estimates. **f,** Final 3D reconstruction colored according to local resolution.

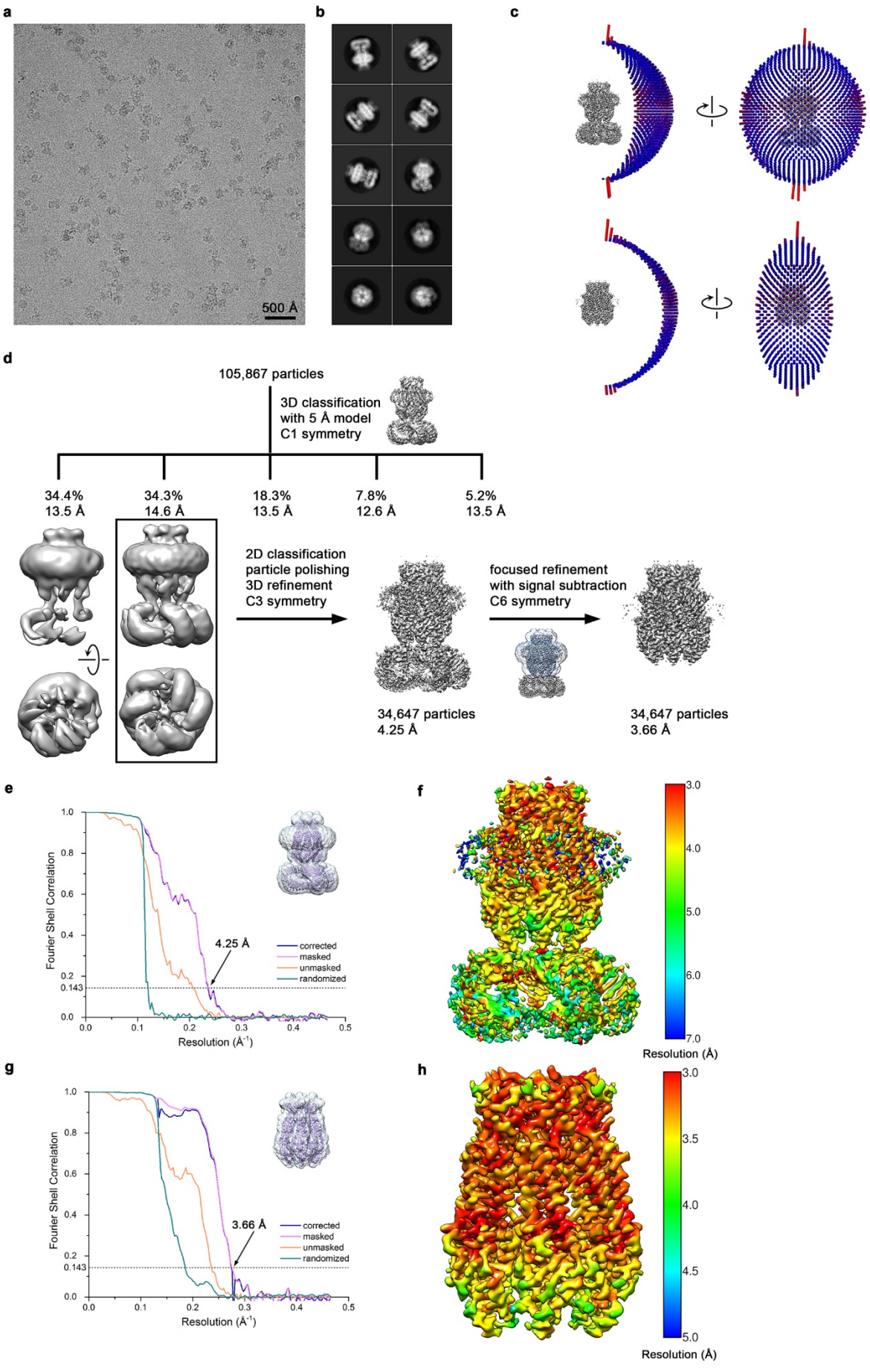
a
500 Å
b
c
d
105,867 particles
3D classification
with 5 Å model
C1 symmetry
34.4%
13.5 Å
34.3%
14.6 Å
18.3%
13.5 Å
7.8%
12.6 Å
5.2%
13.5 Å
2D classification
particle polishing
3D refinement
C3 symmetry
34,647 particles
4.25 Å
focused refinement
with signal subtraction
C6 symmetry
34,647 particles
3.66 Å
e
Fourier Shell Correlation
4.25 Å
corrected
masked
unmasked
randomized
0.143
Resolution (Å-1)
f
3.0
4.0
5.0
6.0
7.0
Resolution (Å)
g
Fourier Shell Correlation
3.66 Å
corrected
masked
unmasked
randomized
0.143
Resolution (Å-1)
h
3.0
3.5
4.0
4.5
5.0
Resolution (Å)

Extended Data Figure 4 | Cryo-EM reconstruction of mLRRC8A at 4.25 Å and its pore domain at 3.66 Å. **a,** Representative cryo-EM micrograph of dataset 2 obtained at an FEI Titan Krios and **b,** 2D class averages of mLRRC8A. **c,** Angular distribution plots of all particles included in the final C3-symmetrized full-length reconstruction (upper panel) and the final C6-symmetrized PD reconstruction from focused refinement (lower panel) show uniform orientations. Length and color of cylinders correspond to the number of particles with respective Euler angles. **d,** Data processing workflow. 3D classification was performed directly on the initial set of particles in order to include less-populated orientations, which could be otherwise excluded if subjected to prior 2D classification. One of two predominant classes (boxed) revealed a subset of homogeneous particles, which were used in further processing. The distribution of all particles (%) and the resolution of each class is indicated. The focused refinement with C6 symmetry improved the resolution of the PD. Inset shows the mask applied to the map during refinement, where the particle signal outside the mask, corresponding to the LRRDs, was subtracted **e,** Fourier Shell Correlation (FSC) plot of the final refined unmasked (orange), masked (pink), phase-randomized (green) and corrected for mask convolution effects (blue) cryo-EM density map of C3-symmetric mLRRC8A. The resolution at which the FSC curve drops below the 0.143 threshold is indicated. Inset shows the atomic model within the mask that was applied for calculations of the resolution estimates. **f,** Final 3D reconstruction of the full-length mLRRC8A colored according to its local resolution. **g,** as in **e,** but for the 3D reconstruction of the C6-symmetric PD. **h,** as in **f,** but for the 3D reconstruction of the PD.

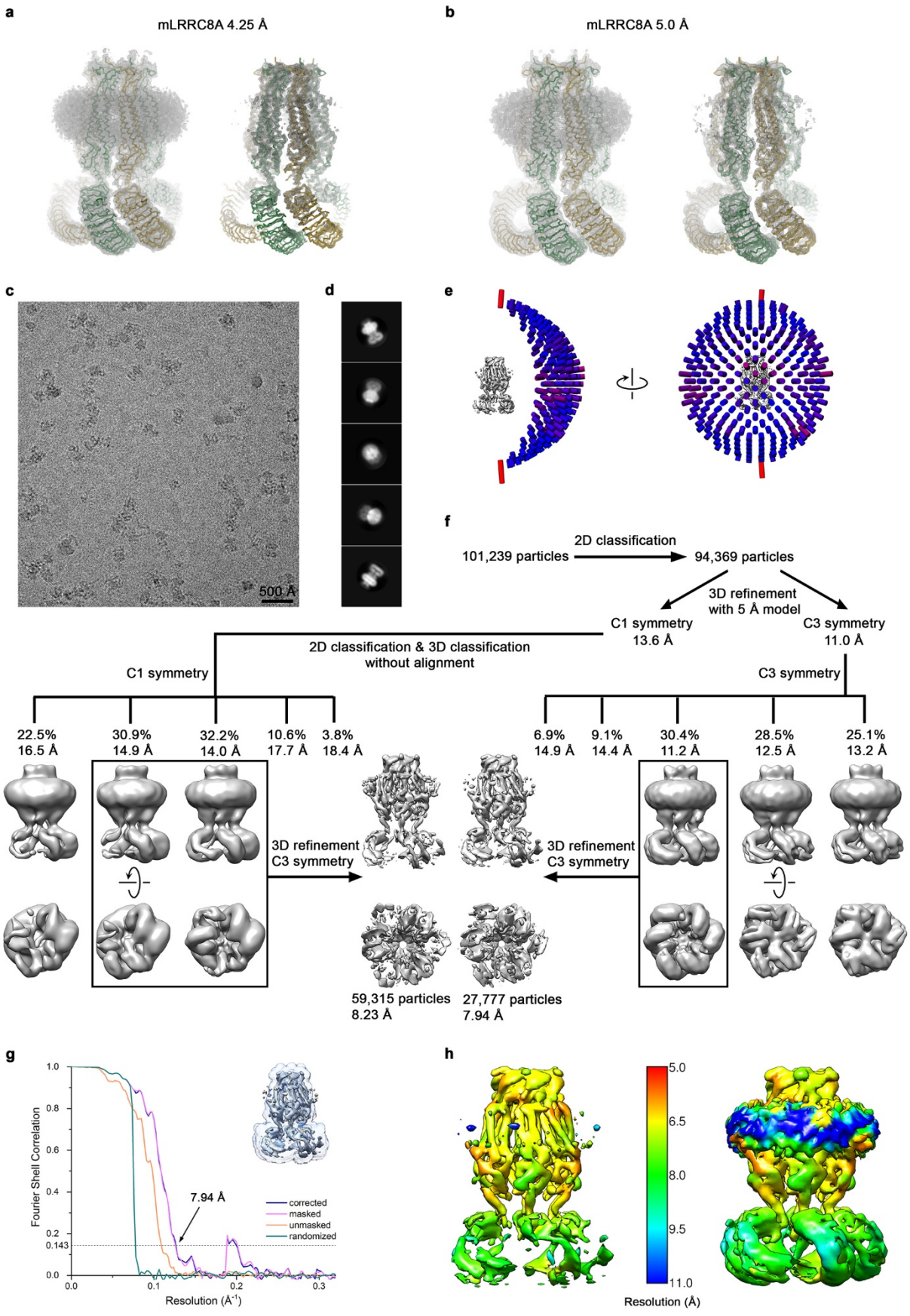
a
mLRRC8A 4.25 Å
b
mLRRC8A 5.0 Å
c
500 Å
d
e
f
2D classification
101,239 particles
94,369 particles
3D refinement
with 5 Å model
C1 symmetry
13.6 Å
C3 symmetry
11.0 Å
2D classification & 3D classification
without alignment
C1 symmetry
C3 symmetry
22.5%
16.5 Å
30.9%
14.9 Å
32.2%
14.0 Å
10.6%
17.7 Å
3.8%
18.4 Å
6.9%
14.9 Å
9.1%
14.4 Å
30.4%
11.2 Å
28.5%
12.5 Å
25.1%
13.2 Å
3D refinement
C3 symmetry
3D refinement
C3 symmetry
59,315 particles
8.23 Å
27,777 particles
7.94 Å
g
Fourier Shell Correlation
Resolution (Å-1)
7.94 Å
corrected
masked
unmasked
randomized
h
Resolution (Å)

Extended Data Figure 5 | Comparison of cryo-EM 3D reconstructions of mLRRC8A and mLRRC8A/C. a, Cα-representation of the refined model of mLRRC8A with cryo-EM density at 4.25 Å at low (4.0 σ, left) and high (6.0 σ, right) contour threshold superimposed. **b,** Cα-representation of the refined model of mLRRC8A with cryo-EM density at 5.01 Å at low (7.0 σ, left) and high (9.7 σ, right) contour threshold superimposed. **c,** Representative cryo-EM micrograph of dataset 3 acquired with an FEI Tecnai G^2 Polara microscope. **d**, 2D class averages of the mLRRC8A/C assembly. mLRRC8A/C heteromers were obtained from the co-expression of the two constructs in HEK293 cells followed by a tandem affinity purification to select channels containing both subunits. **e**, Angular distribution plot of all particles included in the final C3-symmetrized reconstruction shows uniform orientations. The length and the color of cylinders correspond to the number of particles with respective Euler angles. **f,** Workflow of mLRRC8A/C data processing. After 3D classification with either C1 or C3 symmetry imposed, the three predominant classes show a symmetric PD and LRRDs with higher flexibility. Cryo-EM density represents an average of mLRRC8A and C subunits, which due to their strong sequence relationship are essentially identical in structure at the current resolution of the data. The final refined C3-symmetrized reconstructions reveal the overall architecture of the hexameric protein, which exhibits very similar features as the mLRRC8A homo-hexamer. Although the final C3-symmetric model generated from non-symmetrized 3D-classes contains twice the number of particles, its resolution is lower compared to the model calculated from the predominant symmetrized 3D class. We thus used latter for structural descriptions. The distribution of all particles (%) and the resolution of each class is indicated. **g**, Fourier Shell Correlation (FSC) plot of the final refined unmasked (orange), masked (pink), phase-randomized (green) and corrected for mask convolution effects (blue) cryo-EM density map of mLRRC8A/C. The resolution at which the FSC curve drops below the 0.143 threshold is indicated. Inset shows the cryo-EM density within the mask that was applied for calculations of the resolution estimates. **h,** Final 3D reconstruction at high (left) and low (right) thresholds colored according to local resolution.

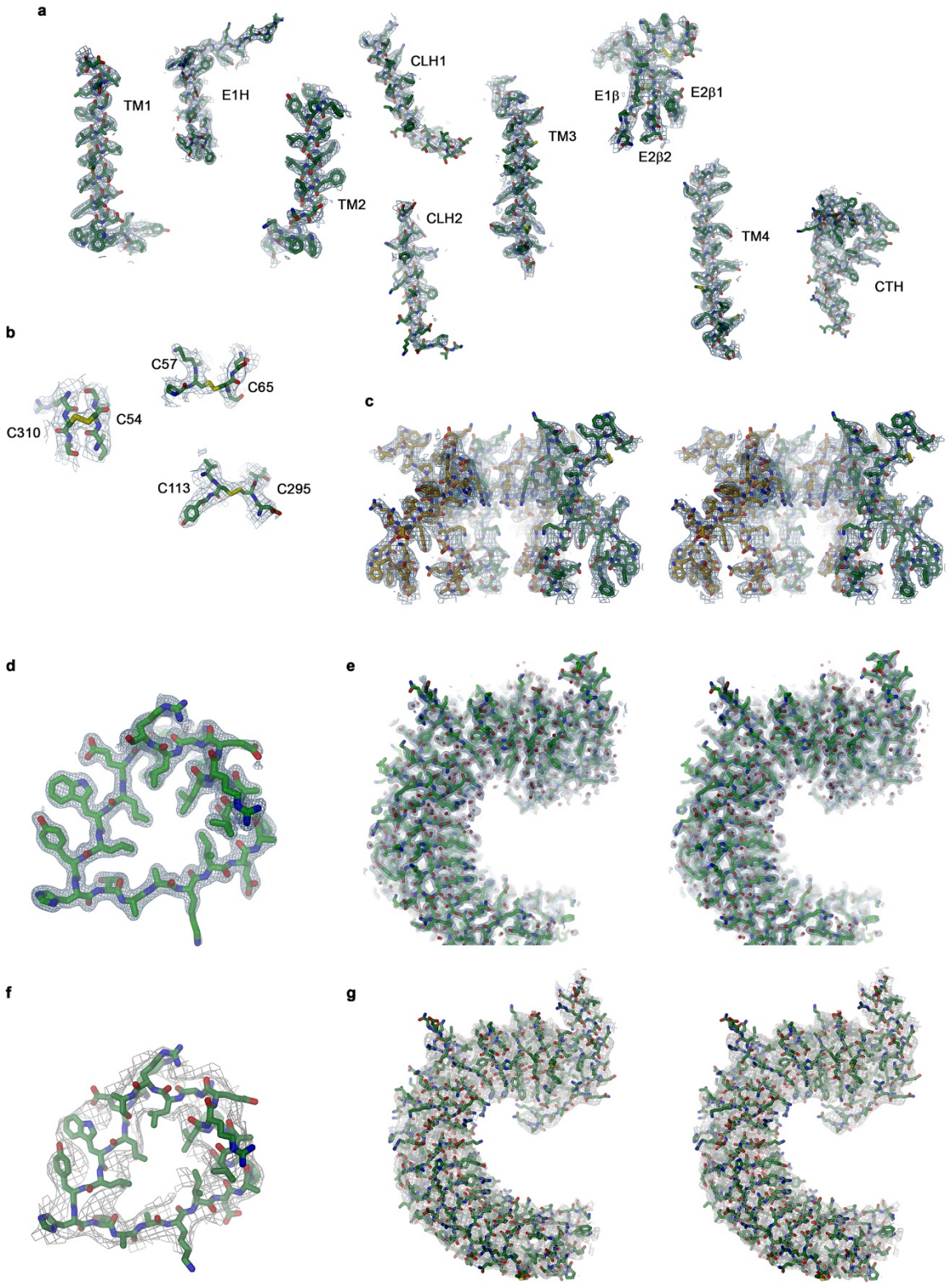

Extended Data Figure 6 | Cryo-EM and X-ray electron density. a, Sections of the cryo-EM density (grey, 6.5 σ) superimposed on the refined structure of the PD. Secondary structure elements are labeled. **b,** Cryo-EM density (grey, 6.0 σ) around disulfide bonds in the ESD. **c,** Stereo view of cryo-EM density (6.5 σ) of the pore region in the ESD with front subunits removed for clarity. **a–c** show cryo-EM density of the C6-symmetrized PD of

mLRRC8A at 3.66 Å. **d,** Section and **e,** stereo view of the isolated LRR domain of mLRRC8A. Electron density (1.0 σ) of the LRR domain determined by X-ray crystallography at 1.8 Å is shown superimposed on the model. **f,** Section and **g,** stereo view of the LRR domain in the full-length mLRRC8A channel. C3-symmetrized cryo-EM density (4.0 σ) is shown superimposed on the model. Whereas the resolution of the entire reconstruction is 4.25 Å, the local resolution of the LRR domains is lower. **a–g** Structures are shown as sticks.

a

X-ray data collection, phasing and refinement statistics (MIR)

	Anomalous dataset	Native dataset (PDB 6FNW)
Data collection		
Space group	$P6_5$ (170)	$P6_5$ (170)
Cell dimensions		
a, *b*, *c* (Å)	140.3, 140.3, 41.9	140.1, 140.1, 42.3
α,*β*,*γ* (°)	90, 90, 120	90, 90, 120
Resolution (Å)	40.45-2.5	40.45-1.8
R_{merge}	9.1 (67.9)	6.5 (158.3)
$I / \sigma I$	79.9 (13.4)	27.1 (2.3)
Completeness (%)	99.3 (93.7)	100.0 (99.9)
Redundancy	154.2 (123.3)	20.2 (19.8)
Refinement		
Resolution (Å)		1.8
No. reflections		43,155
R_{work} / R_{free}		17.9 (20.8)
No. atoms		
Protein		3,426
Ligand/ion		4
Water		337
B-factors		
Protein		47.5
Ligand/ion		73
Water		57.5
R.m.s deviations		
Bond lengths (Å)		0.013
Bond angles (°)		1.27

*Values in parentheses are for highest-resolution shell.

b

Cryo-EM data collection, refinement and validation statistics

	Dataset 1 mLRRC8A^{FL} (EMD-4366) (PDB 6G9L)	Dataset 2 mLRRC8A^{FL} (EMD-4367) (PDB 6G9O)	Dataset 2a mLRRC8A^{PD} (EMD-4362) (PDB 6G8Z)	Dataset 3 mLRRC8A/C (EMD-4361)
Data collection and processing				
Microscope	FEI Tecnai G^2 Polara	FEI Titan Krios		FEI Tecnai G^2 Polara
Camera	Gatan K2 Summit + GIF	Gatan K2 Summit + GIF		Gatan K2 Summit + GIF
Magnification	37,313	46,511		37,313
Voltage (kV)	300	300		300
Electron exposure (e$^-$/Å^2)	70	70		70
Defocus range (μm)	-0.5 to -3.2	-0.5 to -3.2		-0.5 to -3.2
Pixel size (Å)	1.34(0.67)	1.075(0.5375)		1.34(0.67)
Initial particle images (no.)	329,624	105,867		101,239
Final particle images (no.)	54,861	34,674		27,777
Symmetry imposed	C3	C3	C6	C3
Map resolution (Å)	5.01	4.25	3.66	7.94
FSC threshold 0.143				
Map resolution range (Å)	3.0-7.0	3.0-6.0	3.0-4.5	5.0-9.5
Refinement				
Model resolution (Å)	5.3	4.3	3.7	
FSC threshold 0.5				
Model resolution range (Å)	194-5.01	206-4.25	129.0-3.66	
Map sharpening b-factor (Å^2)	-173	-118	-92	
Model composition				
Non-hydrogen atoms	35,532	35,532	15,966	
Protein residues	4,308	4,308	1,908	
B factors (Å^2)				
Protein	292	155	83	
Refmac FSC_{avg}/Rfactor	0.805/0.261	0.717/0.384	0.857/0.301	
R.m.s. deviations				
Bond lengths (Å)	0.004	0.005	0.006	
Bond angles (°)	0.793	0.798	0.826	
Validation				
MolProbity score	1.71	1.66	1.21	
Clashscore	6.04	5.15	1.50	
Poor rotamers (%)	0.08	0.08	0.34	
Ramachandran plot				
Favored (%)	94.52	94.36	95.46	
Allowed (%)	5.48	5.64	4.54	
Disallowed (%)	0	0	0	

*Values in parentheses indicate the pixel size in super-resolution.

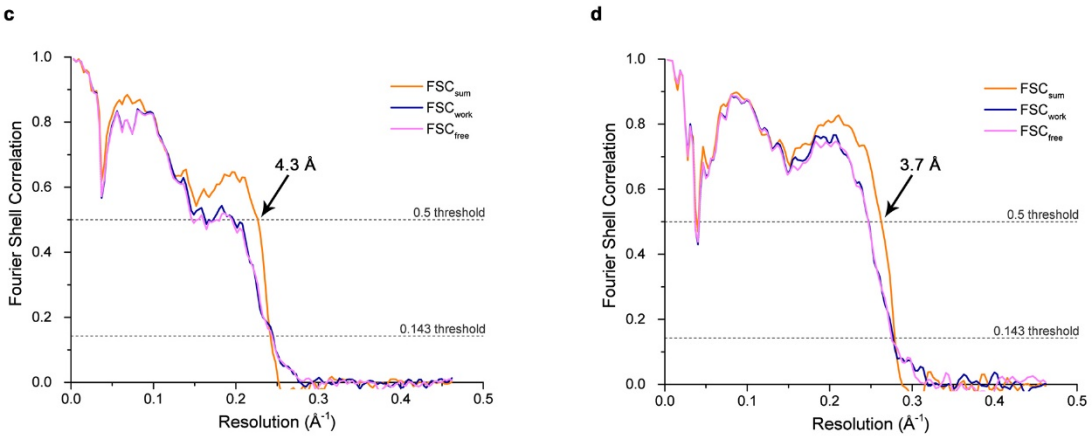

Extended Data Figure 7 | X-ray crystallography and cryo-EM statistics and model validation. a, Statistics of X-ray data collection, phasing and refinement. **b,** Statistics of cryo-EM data collection, processing and model refinement. **c–d,** FSC plots of refined atomic models against the cryo-EM density maps of the full-length protein at 4.25 Å (**c,** dataset 2) and the PD of mLRRC8A at 3.66 Å (**d,** focus-refined dataset 2a). FSC_{sum} (orange) is calculated for the full masked map and the model refined against the complete dataset, FSC_{work} (blue) is calculated for the masked half-map 1 and the shaken model refined against the dataset comprising the half map 1, FSC_{free} (pink) is calculated for the masked half-map 2 and the shaken model refined against the half map 1. FSC thresholds at 0.5 and 0.143 were used for FSC_{sum} and FSC_{work}/FSC_{free}, respectively.

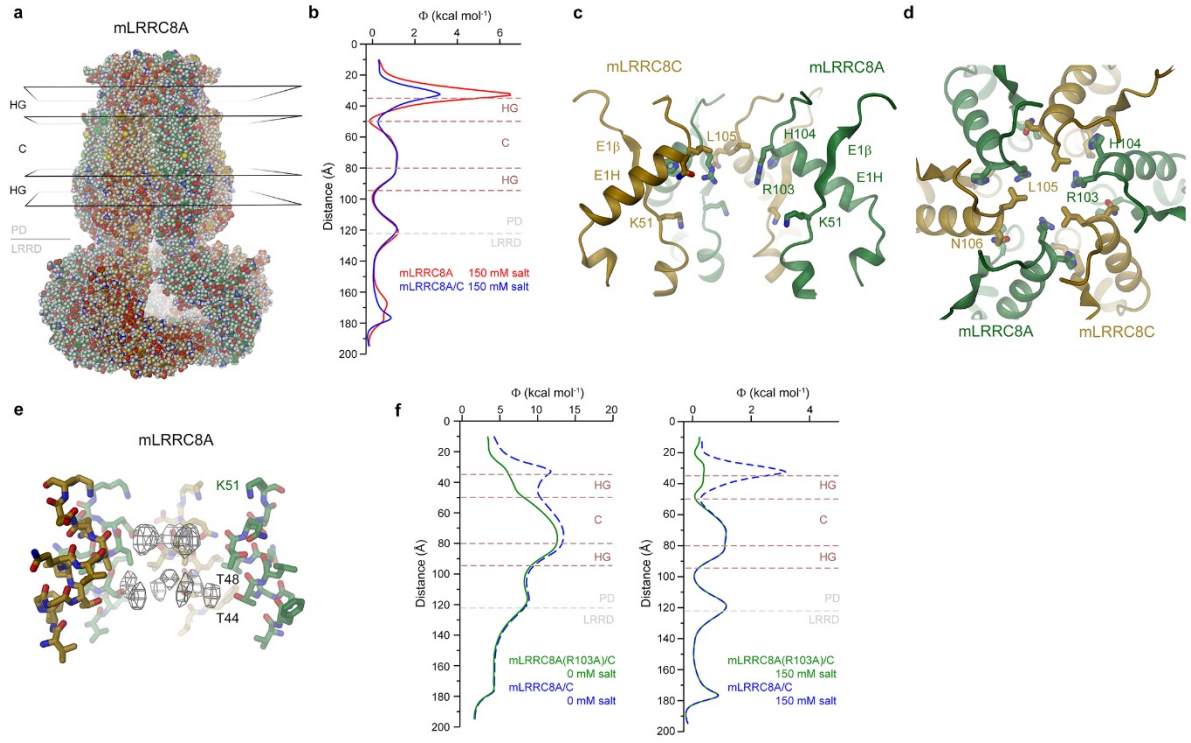

Extended Data Figure 8 | Homology model and electrostatics. a, Model of mLRRC8A used for electrostatic calculations. The high sequence conservation between paralogs and the structural similarity between homo- and heteromeric channels has allowed the construction of a homology model of mLRRC8A/C. Whereas in this model the general features of mLRRC8C are reliably represented, the alternate arrangement of A and C subunits in the hexameric channel, while plausible, is at this stage speculative. In both structures, the missing residues on the respective N-termini were modeled in a way that they do not obstruct the pore. Membrane boundaries (C, hydrophobic core and HG, headgroup regions) are indicated. **b,** Electrostatic potential along the pore of mLRRC8A (red) and mLRRC8A/C (blue) as determined by a numerical solution of the Poisson-Boltzmann equation at 150 mM of monovalent ions in the solvent and the pore region. **c–d,** Part of the ESD of the mLRRC8A/C model lining the pore viewed from within the membrane with front subunits removed for clarity (**c**) and from the extracellular side (**d**). The protein is displayed as ribbon, selected side chains as sticks. Subunits A and C are shown in green and orange, respectively. Whereas in the pore domain of this model most of the interaction interface is conserved, differences of pore-lining residues alter the electrostatic properties of the ion conduction path. **e,** Residual density (5.0 σ) in the pore region of the C3-symmetrized cryo-EM map of mLRRC8A. Panel shows region around T44 and T48 with front subunits removed for clarity. View is as in **c** and protein is displayed as sticks. **f,** Electrostatic potential along the pore of the mLRRC8A(R103A)/C mutant (green) as determined by a numerical solution of the Poisson-Boltzmann equation in the absence (left) and at 150 mM of monovalent ions in the solvent and the pore region (right). **b, f,** Membrane boundaries and the border between PD and LRRD are indicated.

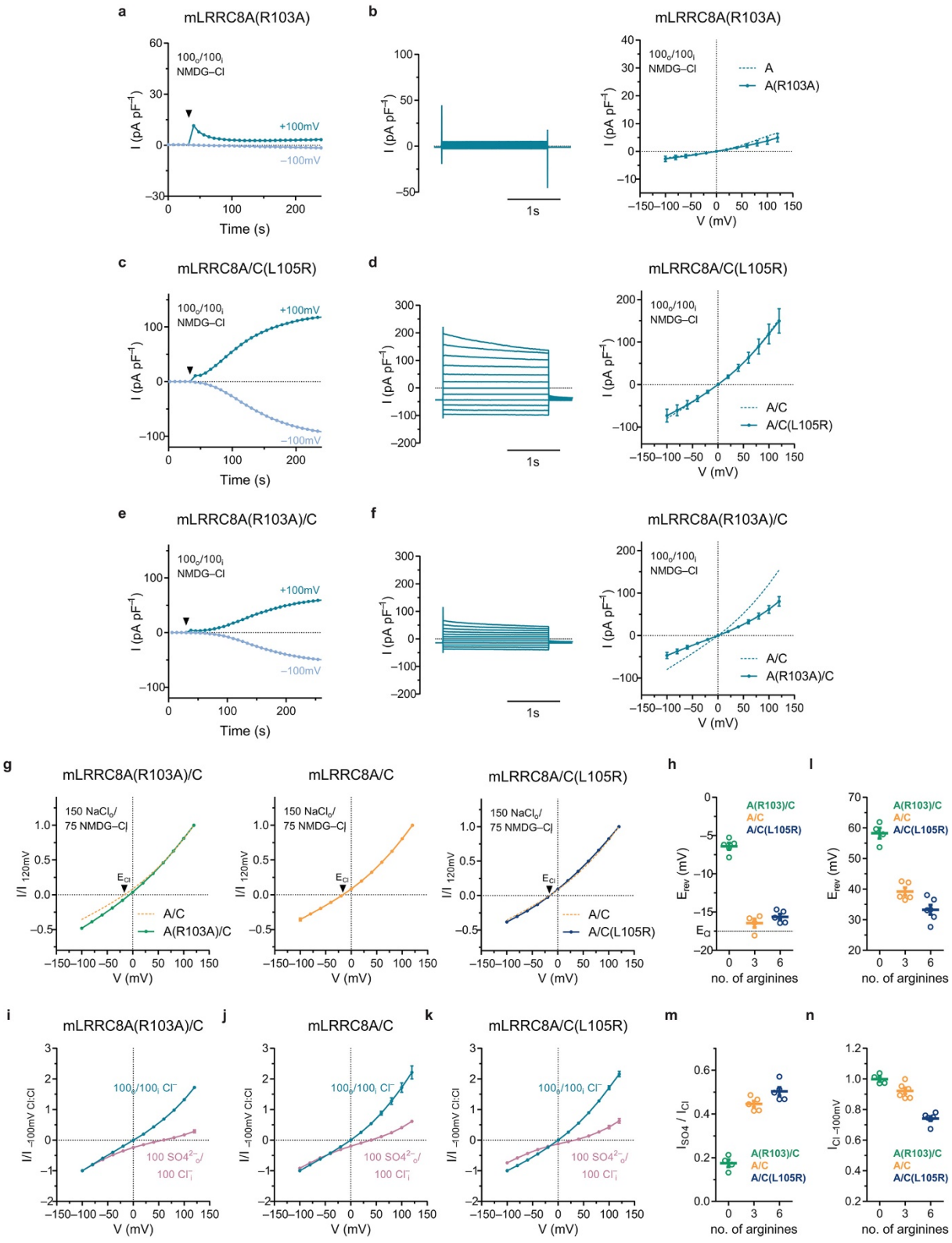

Extended Data Figure 9 | Electrophysiology of selectivity filter mutants. a, Time-dependent response and **b,** current-voltage relationship of *LRRC8*$^{-/-}$ cells expressing mLRRC8A(R103A). **c,** Time-dependent response and **d,** current-voltage relationships of *LRRC8*$^{-/-}$ cells expressing mLRRC8A/C(L105R). **e,** Time-dependent response and

f, current-voltage relationships of *LRRC8*$^{-/-}$ cells expressing mLRRC8A(R103A)/C. **a, c, e,** Black triangle indicates the point of break-in. **b, d, f,** Traces show representative data recorded at the maximum response at the indicated symmetric Cl^- concentrations. Current-voltage relationships show averages of four to seven independent experiments, errors are SEM. **g,** Current-voltage relationships of mLRRC8A(R103A)/C, mLRRC8A/C and mLRRC8A/C(L105R) in the indicated ionic gradient. **h,** Reversal potentials measured from the current-voltage relationship shown in (**g**). **g, h,** The Nernst potential of Cl^- is indicated. **i, j, k,** Current-voltage relationships of the indicated constructs with different extracellular anions. **l,** Reversal potentials measured from the current-voltage relationship shown in **i**, **j** and **k**. **m,** Ratio of the outward ($SO4^{2-}$) and inward (Cl^-) current at +/–100 mV measured from the current-voltage relationship shown in **i**, **j** and **k**. **n,** Relative inward current amplitude used to scale the normalized current-voltage relationship recorded in the presence of extracellular $SO4^{2-}$ in **i**, **j** and **k**. The shift in the reversal potential when extracellular Cl^- is replaced by SO_4^{2-} and the increase in relative $SO4^{2-}$ current reflect the increase in the relative permeability of the divalent anion as the number of positive charges in the selectivity filter increases. **g–n,** Data show mean of four to five independent experiments, errors are SEM. Data in **a–n** were recorded under voltage-clamp conditions in the whole-cell configuration.

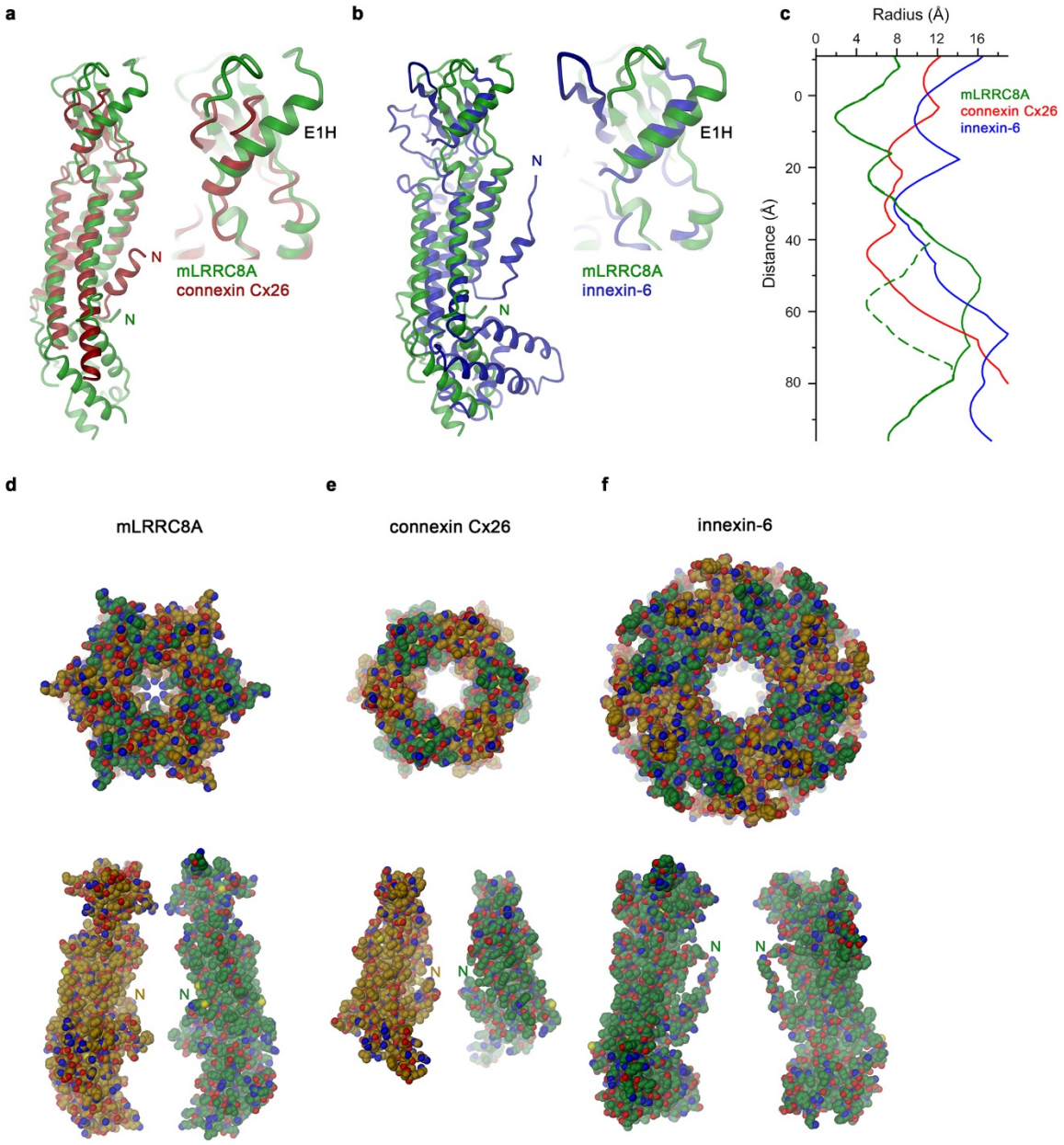

Extended Data Figure 10 | Comparison with gap junction proteins. a, Superposition of subunits of mLRRC8A (green) and connexin Cx26 (PDBID: 2ZW3, red, left) and close-up of the ESD (right). Selected secondary structure elements are indicated. **b,** Superposition of subunits of mLRRC8A (green) and innexin-6 (PDBID: 5H1Q, blue, left) and close-up of the ESD (right). **a, b,** Proteins are displayed as ribbons; selected secondary structure elements are indicated. **c,** Pore radius along the symmetry axis. Dashed green line corresponds to the structure of mLRRC8A containing the modeled N-terminus used for electrostatic calculations. In case of the connexin Cx26, the difference in pore geometry arises from a shortening of helix E1H and in the *C. elegans* innexin-6 from its larger, octameric assembly. **d,** Pore domain of mLRRC8A with modeled N-terminal residues, **e,** connexin Cx26 (PDBID: 2ZW3) and **f,** innexin-6 (PDBID: 5H1Q) viewed from the extracellular side (top) and two opposing subunits of the respective channels shown from within the membrane with N-termini indicated (bottom). **d–f,** Proteins are shown as space-filling models.